Numerical resolution of the inverse source problem for EEG using the quasi-reversibility method

Marion Darbas, Juliette Leblond, Jean-Paul Marmorat, Pierre-Henri Tournier

Numerical resolution of the inverse source problem for EEG using the quasi-reversibility method.

M. Darbas[1], J. Leblond[2], J.-P. Marmorat[3], and P.-H. Tournier[4]

[1] LAGA CNRS UMR 7539, Institut Galilée, 99 avenue Jean-Baptiste Clément, 93430 Villetaneuse, France

[2] Team FACTAS, Centre Inria d'Université Côte d'Azur, BP 93, 06902 Sophia Antipolis Cedex, France

[3] CMA MinesParis, 1 rue Claude Daunesse, CS 10 207, 06904 Sophia Antipolis Cedex, France

[4] Sorbonne Université, CNRS, Université Paris Cité, Inria, Laboratoire Jacques-Louis Lions (LJLL), F-75005 Paris, France

E-mail: darbas@math.univ-paris13.fr

Abstract. We propose a numerical method for solving a family of source estimation inverse problems from Cauchy data for Poisson (conductivity) PDE in non-homogeneous domains. The targeted application is the electroencephalography (EEG) dipolar source localization problem in brain imaging, for which it allows to take into account the specific heterogeneity of the skull in the data transmission step (cortical mapping) from the scalp to the cortex.

Keywords: Inverse problems, elliptic PDE, quasi-reversibility, best constrained approximation, brain imaging (EEG).

Submitted to: *Inverse Problems*

1. Introduction

Electroencephalography (EEG) is a non-invasive cerebral exploration method and one of the most widespread clinical and functional brain imaging techniques. Measurements of the electric potential generated by normal or pathological brain activity are taken at electrodes placed at the surface of the scalp. They record in a passive way the voltage potential fluctuations between different cortical regions. EEG-monitoring can provide periodic and repeated evaluations at the bedside of the patient. The important goal of brain imaging using EEG is to localize cerebral sources within the brain that generate the measured EEG signals on the scalp (together with an appropriate current flux). EEG is known to have an excellent time resolution and is able to record neural events of one millisecond time order. It can be used in presurgical evaluation for refractory epilepsy [6, 38]. Further, it provides a

tool for studying functional brain connectivity, as for instance the development of language networks in children [22]. Note that EEG is the single available clinical process able to follow the premature neonate functional brain development [45].

From a mathematical point of view, source localization from incomplete overdetermined Cauchy-type data is an (ill-posed) inverse problem that aims to determine the location of electric brain sources and their characteristics (moments if the sources are dipolar). A large number of analytical and numerical methods for the source reconstruction exist in the literature (see e.g. [15, 24], references therein and in the sequel of this section). They are intimately linked with the head model (geometry and electric conductivity distribution), and with the modeling of electric brain sources. The forward problem for EEG consists in finding the potential on the scalp for a given electric source located in the brain. Generally, multi-layered head models are considered and the conductivity of each layer (brain, cerebrospinal fluid - CSF, skull, scalp) is assumed to be constant (whence piecewise constant in the overall head). On the one hand, the spherical head model has gathered much interest from the beginning of EEG source analysis since an explicit expression for the potential is available [37]. On the other hand, realistic head models obtained from the segmentation of anatomical images using magnetic resonance imaging (MRI) are able to take into account the geometrical complexity of the different tissues [40]. Concerning the source modeling, dipolar or distributed sources can be considered. At the frequencies of brain electromagnetic phenomena, the quasi-static approximation of Maxwell equations is valid [26, 36] and the (scalar) electric potential solves the conductivity Poisson partial differential equation (PDE) in the head domain. For the numerical resolution of the forward problem, both boundary elements and 3D finite elements are commonly used. Spherical head models are still the most used ones to solve the forward problem. The accuracy of the EEG source reconstruction depends strongly on the accuracy of the associated forward model.

Source estimation in a domain from data measured at some distance from the source support is a widely addressed inverse problem, in particular for brain imaging purposes. In addition to EEG data on the scalp, available data may consist in measures of the magnetic field outside the head (magnetoencephalography, MEG, see [26]), or measures of the electric potential inside the head (sEEG). These devices record time varying signals, from which static values at a fixed time instant can be obtained, either by direct sampling or performing time-space signal separation through a singular value decomposition (SVD) and component analyses, see e.g. [19].

Depending on the source model, two big classes of methods implemented in software libraries devoted to the resolution of inverse EEG/MEG problems can be distinguished:
- Minimum Norm Estimation (MNE) methods, where the source term is assumed to be distributed on the cortex surface (within the brain, which should be known from MRI), its amplitude (moments) being unknown. This leads to a number of degrees of freedom much bigger than the number of data. Solutions to this underdetermined linear inverse problem are

obtained by norm minimization of the output error combined with a statistical modelization of the source distibution, see‡ [34].
- Dipolar source estimation methods (of dipole fitting family) use a source model reduced to a few pointwise dipoles, make no assumption on their positions, leading to an overdetermined non-linear problem, see§ [19], [35] (MUSIC, Multiple Signal Classification).

Among the last ones, we focus on the method developed in the software tool FindSources3D‖ (FS3D) which belongs to the (static) dipolefit class in a spherical representation of the head with piecewise homogeneous conductivity. It makes use of an efficient analytic method that allows to retrieve both the number and the characteristics of dipolar sources (locations, moments, even in time correlated situations), see [11]. The approach consists in firstly transmitting the recorded data from the scalp to the cortex, and then in applying a source reconstruction method in the brain. The data transmission issue from the scalp to the cortex amounts to Cauchy problems for Laplace-Poisson PDE whose solutions carry harmonicity properties. They remain ill-posed (additional assumptions are required to ensure existence, uniqueness, and stability of solutions) and have been studied in [5, 11, 21, 26]. The resolution of their regularized versions, of Tykhonov type, can be carried out using boundary element methods on the layers interfaces, with meshes as described in [23, 36] or appropriate families of functions in simple geometrical settings [2, 11, 33]. The data transmission in FS3D from the scalp to the cortex needs the computation of the spherical harmonic coefficients. Then, FS3D makes use of best rational approximation on families of 2-D planar cross-sections in order to locate singularities and to determine the expected quantity of brain electric sources. From those planar singularities, the sources are finally estimated, together with their moment, in a last clustering step. Through this process, FS3D is also able to recover time correlated sources, which is an important advantage with respect to other software tools addressing the same problem.

In the present paper, we propose a numerical method for the EEG inverse source problem which is able to take into account the heterogeneity of the head tissues, in particular of the skull layer, yet under isotropy assumptions (i.e. scalar conductivity). The electric conductivity of the skull can hardly be assumed to be constant because of both hard and spongy bones, especially the presence of fontanels for neonates. Fontanels are tissues that are in the process of ossification. They therefore possess different (inhomogeneous) electric properties in comparison to an homogeneous skull. Furthermore, skull conductivity models vary between individuals [1, 3, 39] and through time for a single person. The inhomogeneity of the skull conductivity prevents the application of boundary element methods which are currently used for EEG source localization. Finite element method is required to model the

‡ And the dedicated software MNE `https://mne.tools/stable`.
§ And the software EEGLAB, `https://sccn.ucsd.edu/eeglab`; see also Brainstorm, `https://neuroimage.usc.edu/brainstorm`, FieldTrip, `https://www.fieldtriptoolbox.org`.
‖ `https://www-sop.inria.fr/apics/FindSources3D/en/`.

skull volume itself. Few reconstruction methods for a varying conductivity are proposed. In [14], a minimization approach using the Broyden-Fletcher-Goldberg-Shanno (BFGS) iterative algorithm is performed with good reconstructions of dipolar sources (position and moment) for realistic geometries. But the sensitivity of the convergence with respect to the initial guess constitutes a disavantage. Furthermore, the number of sources is assumed a priori. Our aim is to adapt the method of FS3D to a varying conductivity in the skull. In such non homogeneous situations, Cauchy transmission issues for the related conductivity PDE have to be solved through the whole corresponding volume, using FEM for realistic geometries. We propose to regularize the Cauchy problems by applying the quasi-reversibility (QR) method. This is a non-iterative approach which was introduced by Lattès and Lions in [32]. It has been successfully adopted and validated for Laplace's equation (see e.g. [7, 9, 10, 17, 29]). Its variational setting is numerically interesting since finite element methods can be used. We generalize it to a varying conductivity.

The paper is organized as follows. In Section 2, we describe the forward and inverse problems for EEG. In Section 3, we present the quasi-reversibility method that transmits the data from the electrodes to the brain surface. In Section 4, the algorithm implemented within the software tool FindSources3D (FS3D) is precised. Section 5 is devoted to the numerical part: synthetic data, numerical validation of the quasi-reversibility method and of the inverse EEG source method with various simulations. A conclusion is provided in Section 6. Finally, Section 7 consists in an Appendix to Section 4.

2. The forward and inverse problems for EEG

2.1. The forward model

In the low frequency range under consideration in EEG measurements, the electromagnetic field satisfies the quasi-static Maxwell equations where the time derivatives are neglected [26, 28]. The head tissues are characterized by the electric permittivity $\varepsilon > 0$, magnetic permeability $\mu > 0$ supposed to be constant and a conductivity σ with positive values. Under the assumption that the constitution laws of the medium are linear, the quasi-static Maxwell equations are given by

$$(i)\ \nabla \cdot (\varepsilon \mathbf{E}) = \rho\,,\ (ii)\ \operatorname{curl} \mathbf{E} = 0\,,\ (iii)\ \operatorname{curl} \mathbf{H} = \mathbf{J}\,,\ (iv)\ \nabla \cdot (\mu \mathbf{H}) = 0\,, \tag{1}$$

and model the interaction between the electric field $\mathbf{E}$, the magnetic induction $\mathbf{B}$, and the current density $\mathbf{J}$, that are $\mathbb{R}^3$-valued quantities, while the charge density $\rho \in \mathbb{R}$. In the brain and in particular in the cortex, the synchronized effect among a multitude of neurons creates an intracellular current denoted by $\mathbf{J}^s$. The total current density $\mathbf{J}$ produced by cerebral activity splits into two terms (Ohm's law):

$$\mathbf{J} = \sigma \mathbf{E} + \mathbf{J}^s, \tag{2}$$

the current term in the extracellular region of the brain being described by $\sigma\mathbf{E}$. It follows from (1)-(ii), that the electric field derives from a scalar potential u, i.e. $\mathbf{E} = \nabla u$.
Now, consider a simply connected bounded domain $\Omega \subset \mathbb{R}^3$ with $\mathcal{C}^2$ smooth boundary $\partial\Omega$. Taking the divergence of (1)-(iii) together with (2) yields the following transmission equation for the electric potential u in Ω (in the distributional sense, for distributions $\boldsymbol{J}^s$):

$$-\nabla \cdot (\sigma \nabla u) = \nabla \cdot \boldsymbol{J}^s. \tag{3}$$

In the typical multi-layer head model, we distinguish a number of nested layers corresponding to the brain (containing gray and white matters), maybe to the cerebrospinal fluid (CSF), the skull, and scalp. Therefore, consider a partition of Ω into L open nested subdomains $(\Omega_i)_{i=0,\dots,L-1}$ such that

$$\overline{\Omega} = \bigcup_{i=0}^{L-1} \overline{\Omega}_i \text{ while } \Omega_i \cap \Omega_j = \emptyset\,,\ \forall i \neq j\,,\ \text{and } \overline{\Omega}_i \cap \overline{\Omega}_j = \emptyset\,,\ \forall j \notin \{i-1, i, i+1\}\,.$$

We also assume that Ω_0 coincides with the brain and is simply connected. We denote by $\Omega_L = \mathbb{R}^3 \setminus \bar{\Omega}$ the outside of Ω and by S_i, $i = 0, \dots, L-1$, the interface between Ω_i and Ω_{i+1}. We assume that $(S_i)_i$ are closed $\mathcal{C}^2$ surfaces. Let $\boldsymbol{n}_i$ be the unit normal vector on S_i oriented towards the exterior of Ω_i. We denote by $\Gamma = \partial\Omega$ the exterior boundary of the whole domain Ω. This configuration includes the classical spherical model of three concentric spheres representing brain, skull and scalp (see Figure 1 left).

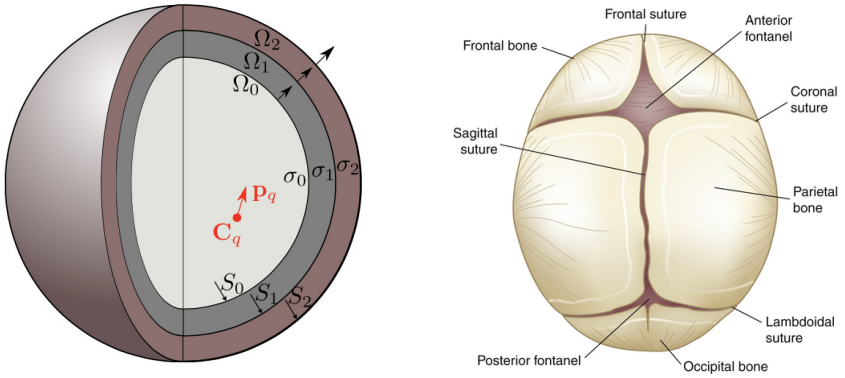

Figure 1. Left: Spherical head model with $L = 3$ and one source $(\mathbf{c}_q, \mathbf{p}_q)$. Right: Fontanels and skull of a neonate.

Let $\sigma_i = \sigma_{|\Omega_i}$ $(i = 0, \dots, L)$ denote the conductivity of the subdomain Ω_i. We set $\sigma_L = 0$ in Ω_L, since the conductivity of the air is zero. We assume that σ_i belongs to $W^{1,\infty}(\Omega_i)$ such that

$$0 < c \leq \sigma_i(\boldsymbol{x}) \leq C < +\infty,\ \boldsymbol{x} \in \Omega_i\,,\ i = 0, \dots, L-1\,.$$

The space $W^{1,\infty}(\Omega_i)$ coincides with the space of Lipschitz continuous functions on $\bar{\Omega}_i$. This assumption on the conductivity is one of the main features of this work. It allows in particular

to take into account the specific heterogeneity of the skull layer. Indeed, if the piecewise constant conductivity assumption is relevant for tissues of the brain and scalp (and CSF), it is not the case of the skull, whose conductivity actually varies. For instance, the skull's structure could be modelled by a spongiosa part (soft bone) located between inner and outer compacta parts (hard bone) [39]. For the neonates, the presence of fontanels in the skull (see Figure 1 right) could be modeled also through a varying conductivity [3].

The source model of neural activity can be described by a sum of Q electric dipoles located in the brain (e.g. [26, 44]). Each dipole is characterized by its position $\boldsymbol{c}_q \in \Omega_0$ and its moment $\boldsymbol{p}_q$ which is a vector of $\mathbb{R}^3$. The points $(\boldsymbol{c}_q)_q$ are assumed to be mutually distinct and the vectors $\boldsymbol{p}_q$ are non vanishing, i.e.

$$\boldsymbol{c}_q \neq \boldsymbol{c}_s \quad \forall q \neq s \quad \text{and} \quad \boldsymbol{p}_q \neq 0 \quad \forall q, s \in \{1, \ldots, Q\}.$$

The current density $\boldsymbol{J}^s$ thus reads:

$$\boldsymbol{J}^s = \sum_{q=1}^{Q} \boldsymbol{p}_q \delta_{\boldsymbol{c}_q}$$

where $\delta_{\boldsymbol{c}_q}$ denotes the Dirac distribution supported at $\boldsymbol{c}_q$. The r.h.s. of (3) is then given by

$$F = \nabla \cdot \boldsymbol{J}^s = \sum_{q=1}^{Q} \boldsymbol{p}_q \cdot \nabla \delta_{\boldsymbol{c}_q}. \tag{4}$$

Since $\sigma_L = 0$, no electric current can flow out of the head in Ω_L and the electric potential u is then solution of the following boundary problem with an homogeneous Neumann condition

$$-\nabla \cdot (\sigma \nabla u) = F \text{ in } \Omega, \ \sigma \partial_{\boldsymbol{n}} u = 0 \text{ on } \Gamma. \tag{5}$$

For given sources $(\boldsymbol{c}_q, \boldsymbol{p}_q) \in \Omega_0 \times \mathbb{R}^3$, $q = 1, \ldots, Q$, and a known distribution of the conductivity σ in Ω, computing a solution u to problem (5) is the forward problem for EEG. Notice that (5) includes the following transmission conditions (jumps) on any interface S_i, $i = 0, \ldots, L-1$,

$$0 = [u]_{|S_i} = u^-_{|S_i} - u^+_{|S_i}, \ 0 = [\sigma \partial_{\boldsymbol{n}} u]_{|S_i} = \sigma_i \partial_{\boldsymbol{n}} u^-_{|S_i} - \sigma_{i+1} \partial_{\boldsymbol{n}} u^+_{|S_i}. \tag{6}$$

A direct variational formulation of (5) in $H^1(\Omega)$ is not possible since the source term F belongs to the Sobolev space $H^s(\mathbb{R}^3)$ for $s < -5/2$. In order to overcome this difficulty, we apply the subtraction approach [3, 21, 46]. It consists of decomposing the potential u, solution to (5), into a potential $\tilde{u}$ which contains the singularities and a regular lifting w :

$$u = \tilde{u} + w, \text{ with } \tilde{u} = \sum_{q=1}^{Q} \tilde{u}_q. \tag{7}$$

With a view to define the singular potentials $\tilde{u}_q$, we assume that the brain conductivity σ_0 is constant in a neighborhood of each source (see [3] for details). More precisely we fix a family of disjoint open balls $(\mathcal{V}_q)_{q=1,\dots,Q}$ such that $\mathcal{V}_q \subsetneq \Omega_0$, $\boldsymbol{c}_q \in \mathcal{V}_q$ and

$$\sigma_{0|\mathcal{V}_q} \equiv \alpha_q = \sigma_0(\boldsymbol{c}_q) \in \mathbb{R}, \quad \text{for any} \quad q \in \{1, \dots, Q\}. \tag{8}$$

The singular potential $\tilde{u}_q$ is solution of the following Poisson equation

$$-\alpha_q \Delta \tilde{u}_q = \boldsymbol{p}_q \cdot \nabla \delta_{\boldsymbol{c}_q} \text{ in } \mathbb{R}^3. \tag{9}$$

It can be obtained by convolution of the fundamental solution of the Laplace equation with $\dfrac{1}{\alpha_q}\boldsymbol{p}_q \cdot \nabla \delta_{\boldsymbol{c}_q}$ as follows

$$\tilde{u}_q(\boldsymbol{x}) = \frac{1}{4\pi\alpha_q} \boldsymbol{p}_q \cdot \frac{(\boldsymbol{x} - \boldsymbol{c}_q)}{|\boldsymbol{x} - \boldsymbol{c}_q|^3}, \ \forall \boldsymbol{x} \in \mathbb{R}^3 \setminus \{\boldsymbol{c}_q\}. \tag{10}$$

The potential $\tilde{u}_q$ has a singularity at the source point $\boldsymbol{c}_q$, but is smooth everywhere else. The auxiliary function w satisfies the following boundary value problem

$$\begin{cases} -\nabla \cdot (\sigma \nabla w) &= \displaystyle\sum_{q=1}^{Q} \nabla \cdot ((\sigma - \alpha_q) \nabla \tilde{u}_q) \quad \text{in} \quad \Omega, \\ \sigma \partial_{\boldsymbol{n}} w &= -\sigma \displaystyle\sum_{q=1}^{Q} \partial_{\boldsymbol{n}} \tilde{u}_q \qquad\qquad\qquad \text{on} \quad \Gamma. \end{cases} \tag{11}$$

Since problem (11) involves a Neumann boundary condition, its solution is determined up to an additive constant only. We therefore introduce the following subspace of $H^1(\Omega)$

$$H = \left\{ v \in H^1(\Omega) \,\middle|\, \int_\Omega v \, d\mathbf{x} = 0 \right\}.$$

The variational formulation for w then reads as follows:

$$\text{find } w \in H \text{ such that } b(w, v) = l(v) \quad \forall v \in H^1(\Omega), \tag{12}$$

where

$$b(w, v) = \int_\Omega \sigma \nabla w . \nabla v \, d\mathbf{x}$$

is a symmetric linear form on $H^1(\Omega) \times H^1(\Omega)$ and

$$l(v) = \sum_{q=1}^{Q} \int_\Omega (\alpha_q - \sigma) \nabla \tilde{u}_q \cdot \nabla v \, d\mathbf{x} - \sum_{q=1}^{Q} \int_\Gamma \alpha_q \partial_{\boldsymbol{n}} \tilde{u}_q v ds$$

is a linear form on $H^1(\Omega)$. The bilinear form $b(\cdot,\cdot)$ is clearly continuous on $H^1(\Omega)\times H^1(\Omega)$ and H-elliptic. Furthermore, the linear form $l(\cdot)$ is continuous on H. The compatibility condition $l(1)=0$ can be proven with the help of the solid angle formula (see e.g. [31]). Then, Lax-Milgram's theorem guarantees the uniqueness of the solution $w\in H$. We refer to [3, 20] for any details. In [4, Prop. 1, Cor. 1], uniqueness and regularity properties of solutions to the forward problem (5) are established for smooth enough geometries and piecewise constant conductivities, that may extend to varying conductivities. They also use the above decomposition (7) and the strict ellipticity of the operator, together with the De Giorgi-Nash theorem in order to show that $w\in H^1(\Omega)$ is in fact Hölder smooth in Ω.

2.2. The inverse source problem

We denote by $\Gamma^*\subset\Gamma$ an open subset of Γ with $\mathrm{meas}(\Gamma^*)\neq 0$. The inverse problem for EEG consists in reconstructing the source F of the form (4) from a single Dirichlet measurement $f=u_{|\Gamma^*}$ of a solution u to (5) on Γ^*. More precisely, the aim is to determine the quantity Q, the locations $(\boldsymbol{c}_q)$ and moments $(\boldsymbol{p}_q)$, $q=1,\dots,Q$, in the source F generating the data f.

In experiments, a finite number of surface electrodes, on which voltages are recorded, are attached to the boundary. Consider $\mathcal{L}$ well-separated pointwise electrodes $\{\boldsymbol{e}_\ell\}_{\ell=1}^{\mathcal{L}}$ on Γ^*. Measurements are given by

$$u(\boldsymbol{e}_\ell)=f(\boldsymbol{e}_\ell)=U_\ell,\ \ell=1,\dots,\mathcal{L}, \tag{13}$$

with $U=(U_\ell)_{\ell=1}^{\mathcal{L}}\in\mathbb{R}^{\mathcal{L}}$. The function f has to belong to (the trace space) $H^{1/2}(\Gamma^*)$ and is chosen from the measurements U_ℓ as an appropriate interpolant of u at points $\boldsymbol{e}_\ell$. Observe that EEG data U_ℓ are subject to noise and errors, whence the choice of such an f that robustly approximates them is judicious:

$$f(\boldsymbol{e}_\ell)\simeq U_\ell,\ |f(\boldsymbol{e}_\ell)-U_\ell|\to 0 \text{ when the error level } \to 0\,,\ \ell=1,\dots,\mathcal{L}.$$

Concerning the overall inverse problem associated to (5), while the source term appears in divergence form in the right-hand side, its properties very much depend on assumption on the source distribution. In the present situation with pointwise dipoles, the uniqueness of the source term F from available data is established in [21] for a constant conductivity σ. The uniqueness result allows to know if the inverse problem is well posed in the following sense: if two measured potentials coincide on a nonempty subset Γ^*, then, they are generated by the same source of the form (4). Stability considerations are also essential properties in view of a numerical resolution. In [14], uniqueness and stability results have been proven with a varying conductivity. The proof of the uniqueness property is based on the subtraction method (following (7)), and the next regularity result for the potential w, Lemma 1 (see [3] for details).

Lemma 1. *Assume that S_i is of class $\mathcal{C}^2$ for any $i \in \{0, \ldots, L-1\}$. Let $\sigma \in L^\infty(\Omega)$ be such that $0 < \sigma_{\min} \leq \sigma(\boldsymbol{x}) \leq \sigma_{\max}$ for almost any $\boldsymbol{x} \in \Omega$, where $\sigma_{\min}$ and $\sigma_{\max}$ are two given positive constants. In addition, assume $\sigma_i \in W^{1,\infty}(\Omega_i), i = 0, \ldots, L-1$, satisfying condition (8). Let $w \in H^1(\Omega)$ be the solution of the variational problem* (12)*. Then we have $w_{|\Omega_i} \in H^2(\Omega_i)$ for any $i = \{0, \ldots, L-1\}$.*

The proof of the uniqueness also involves the unique continuation result for elliptic equations recalled in Lemma 2 (from [43, Thm 1.4]) with $a_{ii} = \sigma$ and $a_{ij} = 0$ for $i \neq j$.

Lemma 2. *Let $D \subset \mathbb{R}^3$ be a smooth bounded connected open domain. Let γ be a nonempty open set of the boundary ∂D of D. Consider the linear operator*

$$Pu = \sum_{i,j=1}^{3} \frac{\partial}{\partial x_i} a_{ij} \frac{\partial u}{\partial x_j},$$

where $a_{ij} \in W^{1,\infty}(D)$,and (a_{ij}) is a symmetric matrix satisfying the uniform ellipticity condition for some constant $\lambda > 0$

$$\sum_{i,j} a_{ij}(x)\xi_i\xi_j \geq \lambda|\xi|^2 \ \forall x \in D, \forall \xi \in \mathbb{R}^3.$$

If $u \in H^2(D)$ satisfies $Pu = 0$ in D and $u_{|\gamma} = \partial_{\boldsymbol{n}} u_{|\gamma} = 0$, then $u = 0$ in D.

Remark 1. In the remarks following [43, Thm 1.4], it is stated that Lemma 2 holds true for $u \in H^1(D)$. Further, if the conductivity is constant in the layer Ω_i, then a version of this lemma is available from [42] whenever the coefficients a_{ij} in P do not depend on x. It also asserts that the unique continuation result holds true for $u \in H^1(D)$.

We now precise our procedure to numerically solve the inverse source problem for EEG through two steps (Sections 3, 4).

3. Data transmission using the quasi-reversibility method

The first step of the reconstruction method is called the cortical mapping procedure. It deals with the numerical resolution of a data transmission problem for elliptic equations. To this end, we propose to apply the quasi-reversibility method (called hereafter QR method) which provides a regularized solution of Cauchy problems in a bounded domain.

3.1. Presentation of the Cauchy problem

Consider the domain $\omega := \cup_{i=1}^{L-1} \Omega_i = \Omega \setminus \overline{\Omega}_0$. From boundary data $(f, g) \in H^{1/2}(\Gamma^*) \times H^{-1/2}(\Gamma^*)$, the Cauchy problem to be solved is the following: find $u \in H^1(\omega)$ such that

$$\left\{ \begin{array}{rll} \nabla \cdot (\sigma \nabla u) & = 0 & \text{in } \omega, \\ u & = f & \text{on } \Gamma^*, \\ \sigma \partial_{\boldsymbol{n}} u & = g & \text{on } \Gamma^*, \end{array} \right. \tag{14}$$

with a varying conductivity σ. The part Γ^* is called the accessible part of the boundary Γ. The inaccessible part is given by $\Gamma_1 = (\Gamma \setminus \overline{\Gamma^*}) \cup S_0$. The aim is to compute the Cauchy data $(u^+, \partial_{\boldsymbol{n}} u^+)$ on the interior inaccessible part S_0 which is the cortex surface. Then, using the transmission conditions (6), we deduce $u^-_{|_{S_0}} = u^+_{|_{S_0}}$ and $\sigma_0 \partial_{\boldsymbol{n}} u^-_{|_{S_0}} = \sigma_1 \partial_{\boldsymbol{n}} u^+_{|_{S_0}}$.

The Cauchy problem (14) is known to be ill-posed in the sense that it may not possess a solution for arbitrary data (f, g) in $H^{1/2}(\Gamma^*) \times H^{-1/2}(\Gamma^*)$, and that the solution is not stable with respect to the data [25]. On the other hand, if problem (14) admits a solution, it is unique. This is an immediate consequence of unique continuation results for elliptic equations [43] (see Lemma 2 above).

3.2. The quasi-reversibility method

The quasi-reversibility method replaces the ill-posed Cauchy problem with a well-posed variational problem including a small regularization parameter. To solve the Cauchy problem (14), we consider the mixed formulation of the quasi-reversibility method which is constructed and studied for Laplace's equation in [7, 10] and we adapt it to the presence of a varying conductivity. To this end, let us introduce the spaces

$$V = H^1(\omega)\,,\ V_f = \{u \in V\ ;\ u = f \text{ on } \Gamma^*\}\ ,\ \text{and } W = \{\mu \in V\ ;\ \mu = 0 \text{ on } \Gamma_1\}\ .$$

Let $a(\cdot,\cdot)$ be the bilinear form involved in (15) defined on $V \times V$ by

$$a(u,v) := \int_\omega \sigma \nabla u \cdot \nabla v d\boldsymbol{x},\ \text{and let } \langle u, v\rangle_V = \int_\omega \nabla u \cdot \nabla v d\boldsymbol{x}\,.$$

We introduce the linear form $\ell(\cdot)$ defined on W by

$$\ell(v) = \int_{\Gamma^*} g\, v_{|\Gamma^*}\, d\boldsymbol{x}\,.$$

First, let us give the variational formulation of the problem (14).

Lemma 3. *Assume that σ satisfies the hypothesis of Lemma 1. For $f \in H^{1/2}(\Gamma^*)$, if the function $u \in V$ is a solution to* (14)*, then $u \in V_f$ and for all $v \in W$,*

$$a(u,v) = \ell(v). \tag{15}$$

Proof. Let $u \in V$. Using a test-function $v \in V$, and integrating on ω, it follows from the classical Green's theorem that

$$\int_\omega \nabla \cdot (\sigma \nabla u) v d\boldsymbol{x} = -a(u,v) + \int_{\partial\omega} \sigma \partial_{\boldsymbol{n}} u v ds. \tag{16}$$

Hence, if $u \in V$ is a solution to (14), it actually belongs to $u \in V_f$ and satisfies the weak formulation (15) since $\partial\omega = \Gamma^* \cup \Gamma_1$, $\sigma \partial_{\boldsymbol{n}} u_{|\Gamma^*} = g$ and $v \in W$ ($v_{|\Gamma_1} = 0$). □

For regularization purposes, the idea is to solve the following weak mixed formulation: for small $\delta > 0$, find $(u_\delta, \lambda_\delta) \in V_f \times W$ such that

$$\left\{ \begin{array}{rcll} \delta \langle u_\delta, v \rangle_V + a(v, \lambda_\delta) & = & 0, & \forall v \in V_0, \\ a(u_\delta, w) - \langle \lambda_\delta, v \rangle_V & = & \ell(w), & \forall w \in W, \end{array} \right. \tag{17}$$

where δ is a regularization parameter. The regularized solution $(u_\delta, \lambda_\delta)$ tends to $(u, 0)$ when δ tends to 0, where u is solution to (14), as stated in the Theorem 2 below.

Theorem 2. *Let $f \in H^{1/2}(\Gamma^*)$. For any $\delta > 0$, the mixed formulation* (17) *admits a unique solution $(u_\delta, \lambda_\delta) \in V_f \times W$. In addition, we have*

$$\lim_{\delta \to 0} (u_\delta, \lambda_\delta) = (u, 0)$$

in $V_f \times W$, where $u \in V$ is the unique solution of the initial Cauchy problem (14).

Proof. We can apply [10, Thm 2.4]. Indeed, the trace operator on Γ^*, that is $u \in V \mapsto u_{|\Gamma^*} \in H^{1/2}(\Gamma^*)$, is onto. Let us introduce some $r \in V$ such that $r_{|\Gamma^*} = f$. Let us set $\tilde{u}_\delta = u_\delta - r$. Problem (17) can be written as a classical variational formulation: find $(\tilde{u}_\delta, \lambda_\delta) \in V_0 \times W$ such that for all $(v, w) \in V_0 \times W$

$$A_\delta \left((u, \lambda), (v, w) \right) = \ell_\delta((v, w))$$

involving the continuous coercive bilinear form A_δ defined on $(V_0 \times W)^2$ by

$$A_\delta \left((u, \lambda), (v, w) \right) = \delta \langle u, v \rangle_V + a(v, \lambda) - a(u, w) + \langle \lambda, w \rangle_V ,$$

and the linear form $\ell_\delta((v, \mu)) = -\delta \langle r, v \rangle_V - \ell(w) + a(r, w)$ given on $V_0 \times W$. Existence and uniqueness follow from Lax-Milgram's Lemma for any boundary measurement $f \in H^{1/2}(\Gamma^*)$ and for all $\delta > 0$. In addition, if there exists a solution $u \in V_f$ to the Cauchy problem (14), Lemma 1 and 2 ensure that u is unique. The convergence of the sequence $(u_\delta, \lambda_\delta)$ to $(u, 0)$ follows as in [10] since u is the only solution to the variational formulation (15). □

In practice, the data f are noisy and will, in general, not belong to the trace space $H^{1/2}(\Gamma^*)$. The boundary condition $u = f$ on Γ^* has thus to be enforced weakly. Assume that $f \in L^2(\Gamma^*)$.

In this configuration, a relaxed mixed formulation is prescribed in [10]. For a varying conductivity, it reads: find $(u_\alpha, \lambda_\alpha) \in V \times W$ such that

$$\left\{ \begin{array}{rcll} \delta \langle u_\alpha, v \rangle_V + \eta^2 \langle u_{\alpha|_{\Gamma^*}}, v_{|_{\Gamma^*}} \rangle_{L^2(\Gamma^*)} + a(v, \lambda_\alpha) & = & \eta^2 \langle f, v_{|_{\Gamma^*}} \rangle_{L^2(\Gamma^*)}, & \forall v \in V, \\ a(u_\alpha, w) - \langle \lambda_\alpha, w \rangle_V & = & \ell(w), & \forall w \in W, \end{array} \right. \tag{18}$$

where the subscript $\alpha = (\delta, \eta)$ indicates that the solution of (18) depends on the regularization parameter $\delta > 0$ and the relaxation parameter $\eta > 0$. The following theorem holds, with $\| \cdot \|_V = \sqrt{\langle \cdot, \cdot \rangle_V}$.

Theorem 3. *Let $f \in L^2(\Gamma^*)$. For any $\alpha = (\delta, \eta)$ such that $\delta > 0$ and $\eta > 0$, problem* (18) *admits a unique solution $(u_\alpha, \lambda_\alpha) \in V \times W$. In addition, we have*

$$\lim_{\delta \to 0} (u_\alpha, \lambda_\alpha) = (u, 0) \tag{19}$$

in $V \times W$ for any fixed $\eta > 0$. Here, u is the unique solution of the Cauchy problem (14)*. Futhermore, we have the following estimates*

$$\|\lambda_\alpha\|_V \leq \sqrt{\delta} \|u\|_V \quad \forall \eta > 0, \tag{20}$$

$$\|u_{\alpha|_{\Gamma^*}} - f\|_{L^2(\Gamma^*)} \leq \frac{\sqrt{\delta}}{\eta} \|u\|_V. \tag{21}$$

Proof. Problem (18) can be written in the following closed form

$$\begin{cases} \text{Find } (u_\alpha, \lambda_\alpha) \in V \times W \text{ such that} \\ A_\alpha \left((u_\alpha, \lambda_\alpha), (v, w) \right) = L_\alpha \left((v, w) \right) \ \forall (v, w) \in V \times W, \end{cases}$$

where the bilinear form $A_\alpha(\cdot, \cdot)$ and the linear form $L_\alpha(\cdot)$ are defined on $V \times W$ by

$$A_\alpha \left((u, \lambda), (v, w) \right) = \delta \langle u, v \rangle_V + \eta^2 \langle u_{|_{\Gamma^*}}, v_{|_{\Gamma^*}} \rangle_{L^2(\Gamma^*)} + a(v, \lambda) - a(u, w) + \langle \lambda, w \rangle_V \,,$$

and

$$L_\alpha \left((v, w) \right) = \eta^2 \langle f, v_{|_{\Gamma^*}} \rangle_{L^2(\Gamma^*)} - \ell(w).$$

The continuity of $A_\alpha(\cdot, \cdot)$ and $L_\alpha(\cdot)$ is clearly obtained, and coercivity comes from the relation

$$A_\alpha \left((u, \lambda), (u, \lambda) \right) = \delta \|u\|_V^2 + \eta^2 \|u_{|_{\Gamma^*}}\|_{L^2(\Gamma^*)} + \|\lambda\|_V^2 \geq \min(\delta, 1) \|(u, \lambda)\|_{V \times W}^2$$

since the scalar product in W is the one of V. We thus apply Lax-Milgram's Theorem and prove existence and uniqueness of a solution of problem (18).

The solution $u \in V_f$ to the Cauchy problem (14) satisfies (see Lemma 3):

$$a(u, w) = \ell(w) \,, \ \forall w \in W \,. \tag{22}$$

By subtracting (22) from the second equation of problem (18), we get

$$a(u_\alpha - u, w) - \langle \lambda_\alpha, w \rangle_V = 0 \,, \ \forall w \in W. \tag{23}$$

Now, take $v = u_\alpha - u$ in problem (18) and $w = \lambda_\alpha$ in (23) and subtract the latter from the first one. Since we have $u = f$ on Γ^*, this yields the following relation

$$\delta (u_\alpha, u_\alpha - u)_V + \eta^2 \|u_{\alpha|_{\Gamma^*}} - f\|_{L^2(\Gamma^*)}^2 + \|\lambda_\alpha\|_V^2 = 0 \tag{24}$$

which gives

$$\delta \|u_\alpha\|_V^2 + \eta^2 \|u_{\alpha|_{\Gamma^*}} - f\|_{L^2(\Gamma^*)}^2 + \|\lambda_\alpha\|_V^2 \leq \delta \|u_\alpha\|_V \|u\|_V. \tag{25}$$

From (25), we deduce that $\|u_\alpha\|_V \leq \|u\|_V$, i.e. the sequence $(u_\alpha)_\alpha$ is bounded with respect to the two parameters δ and η. We thus get the estimation (20), and the convergence of $(\lambda_\alpha)_\alpha$ to 0 whenever the regularization parameter δ tends to 0. In a same way, we get the estimation (21) on the boundary term. By consequence, the sequence $(u_{\alpha|_{\Gamma^*}})_\alpha$ tends to f if $\lim_{\delta\to 0}\left(\frac{\sqrt{\delta}}{\eta}\right) = 0$, hence for any fixed $\eta > 0$. Finally, let us prove the convergence of the sequence $(u_\alpha)_\alpha$. Since this sequence is bounded in V, it admits a subsequence that weakly converges in V to a limit $\overline{u} \in V$. Passing to the limit in the second equation in (18) yields

$$a(\overline{u}, w) = \ell(w)\,,\ \forall w \in W\,,$$

if $\delta \to 0$. On the one hand, we have

$$\langle u_{\alpha|_{\Gamma^*}}, \varphi\rangle_{L^2(\Gamma^*)} \to \langle \overline{u}_{|_{\Gamma^*}}, \varphi\rangle_{L^2(\Gamma^*)},\ \forall \varphi \in L^2(\Gamma^*),$$

from the weak convergence of $(u_\alpha)_\alpha$ in V. On the other hand, according to (21), $u_{\alpha|_{\Gamma^*}} \to f$ strongly in $L^2(\Gamma^*)$ when $\lim_{\delta\to 0}\left(\frac{\sqrt{\delta}}{\eta}\right) = 0$. Consequently, we get $\overline{u} = f$ on Γ^* and $\overline{u}$ is a solution of the weak Cauchy problem. The uniqueness of the solution yields $\overline{u} = u$.

Then, from (24) , we get

$$\begin{aligned}\|u_\alpha - u\|_V^2 &= \langle u_\alpha, u_\alpha - u\rangle_V - \langle u, u_\alpha - u\rangle_V \\ &= -\frac{\eta^2}{\delta}\|u_{\alpha|_{\Gamma^*}} - f\|_{L^2(\Gamma^*)} - \frac{1}{\delta}\|\lambda_\alpha\|_V^2 - \langle u, u_\alpha - u\rangle_V \\ &\leq -\langle u, u_\alpha\rangle_V + \|u\|_V^2.\end{aligned}$$

Because $(u_\alpha)_\alpha$ weakly converges to u, the above inequality implies the strong convergence, at least for a subsequence. It follows from a standard argument that the whole sequence converges strongly to u. □

Remark 4. In Theorem 3, the estimate (20) indicates a convergence order for the convergence of λ_α to 0 independently from the choice of η. The estimate (21) suggests that large values of η should accelerate the convergence of the trace of u_α on Γ^*.

Numerical validation of the data transmission using the QR method will be addressed in Section 5.

4. Source reconstruction

We have computed approximated Cauchy data on the cortex S_0, transmitted from the scalp through the skull using the QR method from Section 3. The next stage of the approach consists in solving the inverse source problem within the brain Ω_0. For simplicity, we stick to the homogeneous brain situation where the conductivity σ_0 is constant within Ω_0.

Following the model described in Section 2.1, we get from (7) and (10) (with $\alpha_q = \sigma_0$) that the singular part $\tilde{u}$ of the potential u, solution to (5) in Ω_0, is given by:

$$\tilde{u}(\boldsymbol{x}) = \frac{1}{4\pi\sigma_0} \sum_{q=1}^{Q} \boldsymbol{p}_q \cdot \frac{(\boldsymbol{x} - \boldsymbol{c}_q)}{|\boldsymbol{x} - \boldsymbol{c}_q|^3}, \ \forall \boldsymbol{x} \in \mathbb{R}^3 \setminus \{\boldsymbol{c}_q\}. \tag{26}$$

The inverse source problem in Ω_0 reads: from u and $\partial_{\boldsymbol{n}} u$ (or $\sigma_0 \partial_{\boldsymbol{n}} u$) on S_0, estimate the quantity $Q \geq 1$, the source locations $\boldsymbol{c}_q \in \Omega_0$ and their moments $\boldsymbol{p}_q \in \mathbb{R}^3$ for $q = 1, \cdots, Q$.
Assume that Ω_0 is a ball, hence $S_0 = \mathbb{S}_0$, the sphere centered at 0, of radius $r_0 > 0$.
In this spherical setting, we solve the inverse source problem using the following four-steps process, a method which is implemented in the FS3D software¶ [11]. These main bricks are listed as:
Step 1. Anti-harmonic projection.
Step 2. 2D slicing.
Step 3. Rational approximation on 2D circles, singularity lines estimation in 3D.
Step 4. 3D clustering of lines extrema, sources positions and moment tuning.
They are summarized below.

Step 1: Anti-harmonic projection From u and $\partial_{\boldsymbol{n}} u$ on S_0, we get their expansions on the spherical harmonics and that of $\tilde{u}$, see [11, Sec. 3.1.2]. Indeed, for $\max_q |\boldsymbol{c}_q| < r \leq r_0$, u can be expanded on the spherical harmonic function basis $\{r^k\, Y_{k,l}\,,\ r^{-(k+1)}\, Y_{k,l}\}$, $k \geq 0$, $|l| \leq k$ (see [18, Ch. 2]) as:

$$u(r, \theta, \varphi) = \sum_{k \geq 0} \sum_{|l| \leq k} \left(\alpha_{k,l}\, r^k + \beta_{k,l}\, r^{-(k+1)} \right) Y_{k,l}(\theta, \varphi)\,,$$

for some (ℓ^2 summable) real-valued coefficients $\alpha_{k,l}$, $\beta_{k,l}$. Therefore,

$$\tilde{u}(r, \theta, \varphi) = \sum_{k \geq 0} \sum_{|l| \leq k} \beta_{k,l}\, r^{-(k+1)}\, Y_{k,l}(\theta, \varphi)\,,$$

while

$$\partial_{\boldsymbol{n}} u(r, \theta, \varphi) = \sum_{k \geq 0} \sum_{|l| \leq k} \left(k\, \alpha_{k,l}\, r^{k-1} - (k+1)\, \beta_{k,l}\, r^{-(k+2)} \right) Y_{k,l}(\theta, \varphi)\,.$$

Hence, having at our disposal the transmitted values of Cauchy data u and $\partial_{\boldsymbol{n}} u$ on S_0, we can (approximately) compute the expansions

$$u(r_0, \theta, \varphi) = \sum_{k \geq 0} \sum_{|l| \leq k} A_{k,l}(r_0)\, Y_{k,l}(\theta, \varphi)\,,\ \partial_{\boldsymbol{n}} u(r_0, \theta, \varphi) = \sum_{k \geq 0} \sum_{|l| \leq k} B_{k,l}(r_0)\, Y_{k,l}(\theta, \varphi)\,,$$

¶ `https://www-sop.inria.fr/apics/FindSources3D/en/`.

by taking their scalar products with $Y_{k,l}$, and estimate $A_{k,l}(r_0)$ and $B_{k,l}(r_0)$ from which we obtain the coefficients $\beta_{k,l}$ of the above spherical harmonic expansion of $\tilde{u}$. More precisely, we have

$$A_{k,l}(r_0) = \alpha_{k,l}\, r_0^k + \beta_{k,l}\, r_0^{-(k+1)}\,,\ B_{k,l}(r_0) = k\,\alpha_{k,l}\, r_0^{k-1} - (k+1)\,\beta_{k,l}\, r_0^{-(k+2)}\,,$$

from which we could eliminate $\alpha_{k,l}$ and get $\beta_{k,l}$, whence $\tilde{u}$ and $\tilde{u}^2$ on S_0.

Step 2: 2D slicing We consider some properties of the trace on S_0 of the function $\tilde{u}^2$, which is continuous there. Indeed, for all $|c_q| < r_0$, (26) defines $\tilde{u}$ as a continuous function on S_0. Elementary slicing is as follows: consider an arbitrary plane Π_p intersecting S_0 along a circle T_p, boundary of a disk D_p contained in this plane, see Fig. 2. On the circle T_p, get the trace (restriction) of $\tilde{u}^2$ and map it on the boundary $\mathbb{T}$ of the unit disk $\mathbb{D}$ in the complex plane. Considering its complex-valued extension f_p to the complex plane $\mathbb{C}$, we see from (26) that:

$$f_p(z) = \sum_{q=1}^{Q} \frac{\varphi_{p,q}^2(z)}{(z-s_{p,q})^3} + \sum_{\substack{q,k=1\\ q\neq k}}^{Q} \frac{\varphi_{p,q}(z)\,\varphi_{p,k}(z)}{(z-s_{p,q})^{3/2}\,(z-s_{p,k})^{3/2}}\,, \tag{27}$$

which shows the structure of f_p which admits Q triple poles $s_{p,q}$ in $\mathbb{D}$ and Q branchpoints (singularities of order 3/2) located at $s_{p,q}$ as well, if $Q \geq 2$. The functions $\varphi_{p,q}$ are precised in Appendix (Section 7), their products and squares are smooth in $\mathbb{D}$.
Moreover, if $Q = 1$, f_p is rational with a single triple pole in $\mathbb{D}$:

$$f_p(z) = \frac{\varphi_{p,1}^2(z)}{(z-s_{p,1})^3}\,. \tag{28}$$

Useful information about the locations of sources is obtained from the study of the singularities of f_p in $\mathbb{D}$. Details on the link between the singularities of f and the sources locations are provided in Appendix, see also [11].

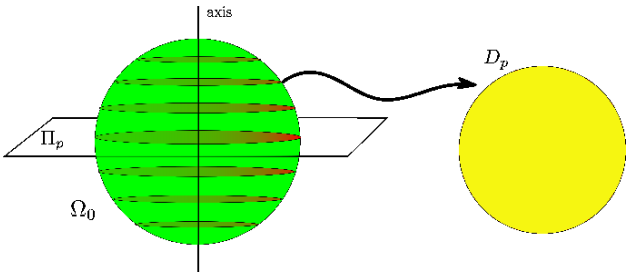

Figure 2. Step 2. 3D to 2D slicing.

The full *2D slicing* algorithm is now as follows: choose two positive integers D and P; choose D directions (axes) Δ_d for $d = 1, \cdots, D$; for each direction Δ_d, choose P parallel

slicing planes $\Pi_{d,p}$ for $p = 1, \cdots, P$. This defines a family of circles $T_{d,p}$ contained in S_0, a family of mappings from the disks $D_{d,p}$ onto $\mathbb{D}$ and together with the related extensions $f_{d,p}$ of $\tilde{u}^2$ from $T_{d,p}$ to $\mathbb{C}$, as explained above, see (27). In order to proceed to the 3D estimation of Step 3, we map back the complex singularities of all the $f_{d,p}$ functions to a set of points inside the 3D ball Ω_0. We typically take $D = 13$, $P = 20$.

Below are the main results, detailed in Appendix and illustrated by Figure 3.

- For fixed p, d, each function $f_{d,p}$ has Q *branched* singularities $s_{d,p,q}$ that are also *poles* of multiplicity 3, see (27) (recall that Q is the quantity of dipolar sources $\boldsymbol{c}_q$).
- For a fixed direction d,
  - the $P \times Q$ singularities $s_{d,p,q}$ for $p = 1, \cdots, P$ are all contained in Q planes, each of these planes containing the axis Δ_d and the source location $\boldsymbol{c}_q$ (whence perpendicular to $\Pi_{d,p}$),
  - in each of these Q planes (for fixed q), the P singularities $s_{d,p,q}$ for $p = 1, \cdots, P$ are linked by a curve (line) that passes through the actual source location $\boldsymbol{c}_q$, at maximum distance from the axis Δ_d.
- Expressions of these theoretical lines are known from (31) and the comments concerning the behaviour of $s_{d,p,q}$.

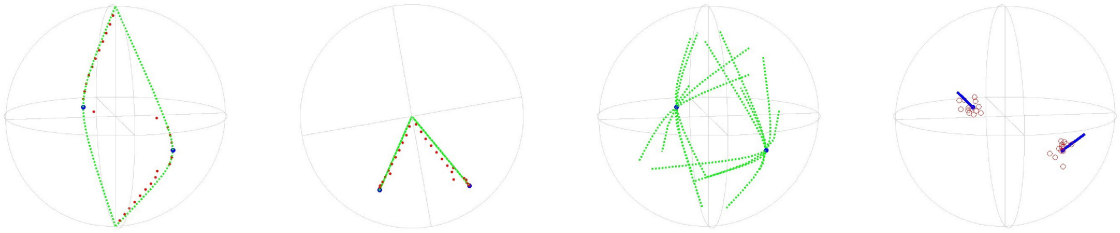

Figure 3. From left to right. (a), (b), Step 3: one direction, $Q = 2$ sources (blue), theoretic singularities (green), estimated poles (red); (c), (d): (c), Step 3, theoretic singularities lines cross at sources locations; (d), Step 4, clustering of estimated positions (red), last least-square locations and moments tuning (blue).

In the following steps, we explain how we use these results in order to estimate the source locations $\boldsymbol{c}_q$ and their moments $\boldsymbol{p}_q$.

Step 3: singularities estimation, rational approximation on circles The estimation of the singularities $s_{d,p,q}$ is performed through best quadratic rational approximation of $f_{d,p}$ given by (27) on $\mathbb{T}$. The approximation function takes the rational form $P(z)/(z-\alpha)^3$, parameterized by its triple pole $\alpha \in \mathbb{D}$ and its numerator P, a polynomial of degree less than 2 with complex-valued coefficients.

The underlying optimization problem concerns 4 complex-valued (or 8 real-valued) parameters and is solved by a standard non-linear minimization algorithm$^+$. The initial guess is estimated either by brute grid evaluation, or by more sophisticated methods relying on the Hankel matrix of the Fourier coefficients of $f_{d,p}$. Whenever $Q = 1$, in the single source situation, each function $f_{d,p}$ is rational with one triple pole of degree 3 and this approach allows to recover the triple pole $s_{d,p,1}$, at least from "exact" data $\tilde{u}^2$, see (28). A nice feature of this process is that it also works out in general for the multiple sources case where $Q > 1$, which it allows to estimate together with the singularities $s_{d,p,q}$, at least when the sources are separated enough (at sufficiently different heights) in the slicing direction d. This is illustrated in Figure 3 (a), (b). On the contrary, the rational approximation error furnishes a criterion allowing to reject the badly identified poles. This algorithm is further quite stable and robust to noise on the data.

Fixed slicing direction: estimate planes of lines, and lines extrema For a fixed direction d, we get a collection of triple poles $\alpha_{d,p}$, $p = 1, \ldots, P$ and their arguments $\arg(\alpha_{d,p}) \in (-\pi, \pi]$. This set is clustered to produce Q estimated angles $\theta_{d,q}$, $q = 1, \ldots, Q$. Each $\theta_{d,q}$ defines with the direction Δ_d a plane that approximately contains the source location $\boldsymbol{c}_q$. In each of these Q clusters, we then look for the maximum modulus $\rho_{d,q}$ of its elements and for the value p which achieve this maximum. Thus $\rho_{d,q}$ and $\theta_{d,q}$ define a point $\hat{\boldsymbol{c}}_{d,q}$ which is an estimation of $\boldsymbol{c}_q$ (related to the direction d). Related to the discussion of Equation (31) in Appendix, which concerns a fixed slicing direction d and a particular singularity z_q, the present $\rho_{d,q}$ is an estimation of the maximum in p of the function noted ρ_p in Appendix and $\theta_{d,q}$ is an estimation of the common argument (independent of p) of the singularities $s_{p,q}$ ($\arg s_{p,q} = \arg z_q$).

Step 4: 3D clustering, final tuning of positions and moments Gathering all the estimations $\hat{\boldsymbol{c}}_{d,q}$ for a family of directions $d = 1, \ldots, D$, form in Ω_0 a collection of points clouds around the Q sources locations $\boldsymbol{c}_q$. Whenever the sources are far enough one from the others in the chosen slicing directions, and the data not too noisy, we indeed obtained $D \times Q$ estimations $\hat{\boldsymbol{c}}_{d,q}$ of the source locations, given by the Q line extrema in D directions. These clouds are separated by a clustering algorithm which returns Q clusters. The mean value (barycenter) of these clusters are furnished as initial values for the estimated positions. Once the source locations are fixed, the data depend linearly on the moment values. A first estimation of these moments is obtained by minimizing the L^2-norm of the residual error at the electrodes (a linear least square problem$^+$. A final non linear least-squares optimization algorithm$^+$ returns both moments and tuned positions (Figure 3, (d)). When true sources are known and their number correctly recovered *, relative position error and angle orientation error

$^+$ Matlab optimization toolbox: `fmincon, lsqlin`.

* This may not always be the case; see Figures 13 and 14.

are computed.

5. Numerical results

In this section, we study the performance of the quasi-reversibility method for data transmission from scalp to cortex together with the source localisation in the cortex using FS3D. We consider the three-layer spherical head model (i.e. $L = 3$, see Figure 1, left). The radii of the brain (Ω_0), skull (Ω_1) and scalp (Ω_2) are respectively 5cm, 5.4cm and 6cm. These sizes correspond to a cranial perimeter of 37.7cm which is approximatively the one of a newborn child. The new approach is tested for several choices of conductivity distribution σ. The conductivities are assumed to be constant in brain and scalp where $\sigma_0 = \sigma_2 = 0.33\text{S.m}^{-1}$. In the skull layer Ω_1, two configurations are modeled and compared: (a) a constant conductivity $\sigma_1 = 0.04\text{S.m}^{-1}$, (b) the presence of the anterior fontanel (see Figure 1 right) and its ossification process by defining the following conductivity function

$$\sigma_1(\boldsymbol{x}) = \sigma_{skull} + (\sigma_f - \sigma_{skull}) g(\boldsymbol{x}) \mathbf{1}_{\Omega_f}(\boldsymbol{x}),\ \boldsymbol{x} = (x_1, x_2, x_3) \in \Omega_1. \tag{29}$$

We fix $\sigma_{skull} = 0.04 S.m^{-1}$ and $\sigma_f = 0.3 S.m^{-1}$ for both the neonatal skull conductivity and the fontanel conductivity [41]. The function g, which is defined by $g(\boldsymbol{x}) = e^{-s(x_1^2+x_2^2)}$, models the process of fontanel ossification. In the numerical experiments hereafter, s is set to 10^4 and thus the fontanel is limited to the region $\Omega_f = \{\boldsymbol{x} \in \Omega_1 \ : \ x_1^2 + x_2^2 \leq r^2\}$ with $r = 10mm$ (see Figure 15).

5.1. Generation of synthetic data

Synthetic data are generated by solving the forward problem (5) (see Section 2.1) for the neonatal head models (a) and (b). The subtraction method is implemented with FreeFem++ (see [27]). Discretization is performed with 3D Finite Elements of type P2. Error estimates are proved in [3]. We use a tetrahedral mesh of the three-layer spherical domain Ω, composed of 617 167 elements.

The measurement region Γ^* on the scalp corresponds to the union of small patches around electrode positions. Three sets of electrode positions with 33, 61 and 257 electrodes are examined (see Figure 4). In practice, the mesh is refined around the electrode positions using the Mmg remeshing software [13]. The surface mesh of the scalp also explicitly includes the boundary of small circular patches representing the electrodes around each electrode position, thanks to the level-set meshing capabilities of Mmg on triangular surface meshes (see Figure 5, left). Then, the synthetic EEG measurement on each electrode patch on the scalp is taken as the average value of the potential on the electrode patch (see Figure 5). The goal is to emulate the features of a real electrode measurement (single value measurement), while avoiding the inaccuracy of interpolating a pointwise measurement on a regular non-adapted finite element mesh.

In the following we will consider two sets of symmetric sources:

- two *distant* sources $\boldsymbol{c}_{q_d} = (2.4, -0.8, 2.9)$ and $\boldsymbol{c}_{q_{-d}} = (-2.4, -0.8, 2.9)$. The respective moments of the sources are $\boldsymbol{p}_{q_d} = (0.9, 0.2, 0.3)J$ and $\boldsymbol{p}_{q_{-d}} = (-0.9, 0.2, 0.3)J$, with intensity $J = 4.1e^{-5}\text{A.m}^{-2}$. These two sources are far away from each other and from the fontanel, and lie at 1.15cm below the brain surface S_0.
- two *close* sources $\boldsymbol{c}_{q_c} = (1, -1, 4)$ and $\boldsymbol{c}_{q_{-c}} = (-1, -1, 4)$ of respective moments $\boldsymbol{p}_{q_c} = (1.2, 1.5, 3.8)J$ and $\boldsymbol{p}_{q_{-c}} = (-1.2, 1.5, 3.8)J$, with intensity $J = 1e^{-5}\text{A.m}^{-2}$. These two sources are close to each other and lie below the fontanel, at 0.76cm below S_0.

Numerical experiments in Sections 5.2 and 5.3 will be performed with one distant source $(\boldsymbol{c}_{q_d}, \boldsymbol{p}_{q_d})$. We will use the two distant sources $(\boldsymbol{c}_{q_d}, \boldsymbol{p}_{q_d})$ and $(\boldsymbol{c}_{q_{-d}}, \boldsymbol{p}_{q_{-d}})$ in Section 5.4. Section 5.6 will present results with one close source $(\boldsymbol{c}_{q_c}, \boldsymbol{p}_{q_c})$, while Sections 5.5 and 5.7 cover the two close sources case $(\boldsymbol{c}_{q_c}, \boldsymbol{p}_{q_c})$ and $(\boldsymbol{c}_{q_{-c}}, \boldsymbol{p}_{q_{-c}})$. Such configurations are relevant for EEG, since the electric activity for a specific task is generally activated on one or two regions of the brain, and here modeled by pointwise dipolar sources.

Figure 4. Electrode positions (side view). From left to right: 33, 61 and 257 electrodes test cases.

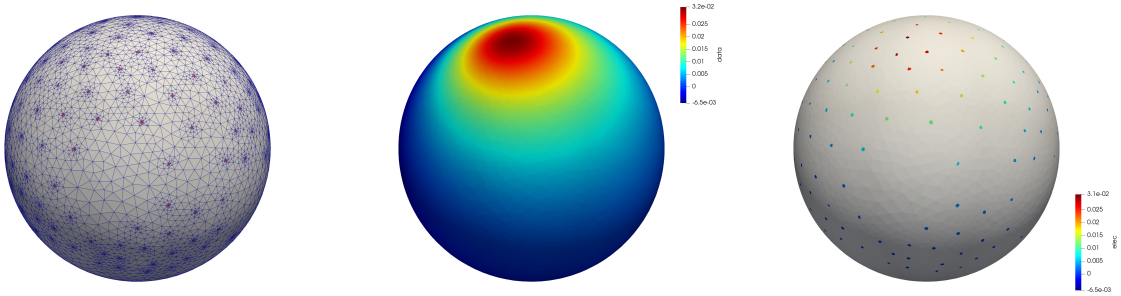

Figure 5. From left to right: mesh adapted to the electrode patches, exact synthetic data on scalp, average value of the potential on each electrode patch used as input data for QR.

5.2. Numerical validation of the quasi-reversibility method

This section is dedicated to validate numerically the data transmission step using the quasi-reversibility method (18). Convergence of the discretized solution to the exact solution is proved in [7, 8] for Laplace's equation and can be generalized to a varying conductivity. One goal is to assess numerically the effect of the regularization and the relaxation parameters δ and η on the quality of the reconstruction of the potential for different noise levels. In the noiseless case, we take $\delta = 10^{-5}$ and we set $\eta = 10^{15}$, which corresponds to an approach with no relaxation (equivalent to (17)). Here we consider one distant source $(\boldsymbol{c}_{q_d}, \boldsymbol{p}_{q_d})$. The source term of the EEG forward problem (5) is thus given by $F = \boldsymbol{p}_{q_d} \cdot \nabla \delta_{\boldsymbol{c}_{q_d}}$ and the data are generated in the way explained in Section 5.1. Numerical solutions of the mixed formulation (18) are obtained using P2 Lagrange finite elements. We implement the quasi-reversibility formulations with FreeFem++ (see [27]). We compare the reconstructed potential, denoted $u^+_{h,\alpha}$, using the quasi-reversibility method with the one u^+_h computed with the forward EEG solver. We measure the error in the reconstructed Dirichlet and Neumann data at the cortex S_0 as

$$e_{D,S_0} = \frac{\|u^+_{h,\alpha|_{S_0}} - u^+_{|_{S_0}}\|_{L^2(S_0)}}{\|u^+_{|_{S_0}}\|_{L^2(S_0)}}, \quad e_{N,S_0} = \frac{\|\partial_{\boldsymbol{n}} u^+_{\alpha|_{S_0}} - \partial_{\boldsymbol{n}} u^+_{|_{S_0}}\|_{L^2(S_0)}}{\|\partial_{\boldsymbol{n}} u^+_{|_{S_0}}\|_{L^2(S_0)}}.$$

First, the accessible part Γ^* is taken as the entire 'upper' half of the scalp S_2 where $z > 0$ instead of the electrode patches. On Figures 6 and 7 we report the relative L^2 errors e_{D,S_0} and e_{N,S_0} for δ varying between 10^{-6} and 10^{-3} and η varying between 10^{-2} and 10^3, for 5% and 20% noise respectively. For 5% noise, the smallest reconstruction error is achieved for $\delta = 10^{-5}$ and $\eta = 1$, with $e_{D,S_0} = 0.11$ and $e_{N,S_0} = 0.221$. For 20% noise, we get the smallest reconstruction errors, $e_{D,S_0} = 0.142$ and $e_{N,S_0} = 0.292$, again for $\delta = 10^{-5}$ and $\eta = 1$. Comparatively, in the noiseless case, the reconstruction error is $e_{D,S_0} = 0.041$ and $e_{N,S_0} = 0.084$.

Now, we consider the configuration with 257 electrodes. Again, we use synthetic data (namely $f = u_{h|_{\Gamma^*}}$ and $g = 0$) and add 5% and 20% white Gaussian noise to the value of the potential at each electrode. We aim at finding the best (δ, η) combination for each of the two noise levels. Figures 8 and 9 show the relative L^2 errors e_{D,S_0} and e_{N,S_0} for 5% and 20% noise respectively. For 5% noise, the smallest reconstruction error is achieved for $\delta = 10^{-4}$ and $\eta = 100$, with $e_{D,S_0} = 0.217$ and $e_{N,S_0} = 0.418$. For 20% noise, we get the smallest reconstruction errors, $e_{D,S_0} = 0.298$ and $e_{N,S_0} = 0.537$, for $\delta = 10^{-4}$ and $\eta = 10$. Comparatively, in the noiseless case, the reconstruction error is $e_{D,S_0} = 0.125$ and $e_{N,S_0} = 0.265$. These values of the regularization and relaxation parameters will be kept throughout the rest of the numerical experiments for noisy synthetic electrode data. As expected, the data transmission is less efficient when the noise level increases. Nevertheless, we will see that the quasi-reversibility method allows to keep the valuable information on the data at the cortex which are needed for the source reconstruction.

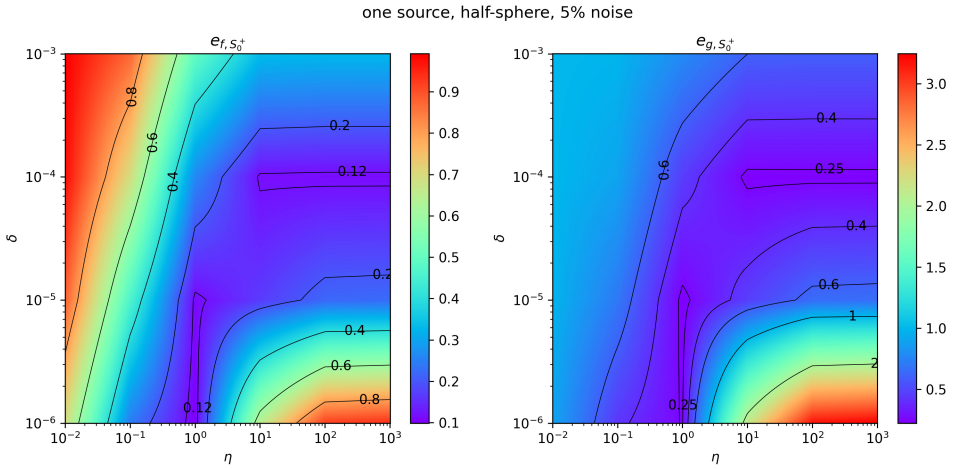

Figure 6. Relative L^2 error of the QR reconstruction in the Dirichlet (left) and Neumann (right) data at the cortex in the half sphere case with 5% noise, for varying values of δ and η.

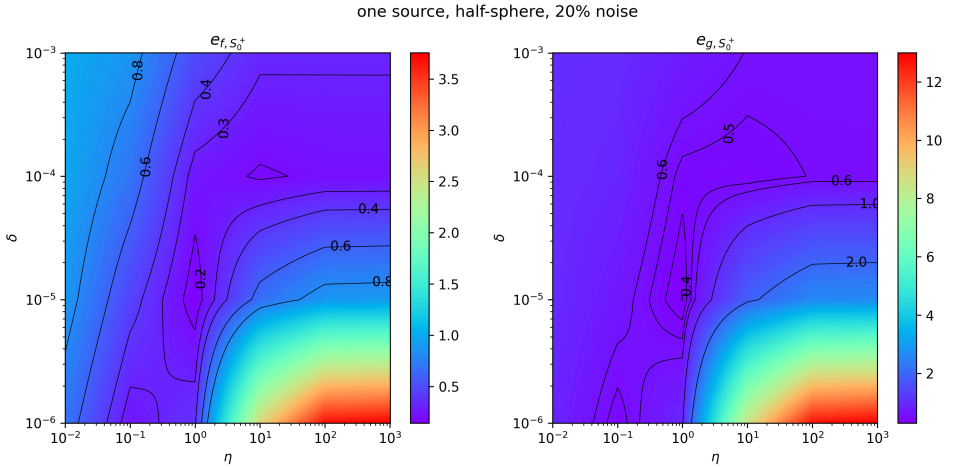

Figure 7. Relative L^2 error of the QR reconstruction in the Dirichlet (left) and Neumann (right) data at the cortex in the half sphere case with 20% noise, for varying values of δ and η.

5.3. One source, no fontanel

We study the whole process in the case of the head model (a) and one distant dipolar source $(\boldsymbol{c}_{q_d}, \boldsymbol{p}_{q_d})$ as in the previous section. QR reconstructions on the cortex along with source reconstruction with FS3D for noiseless data and noisy data with 5% and 20% noise on the value of the potential at each electrode are shown in Figures 10, 11 and 12 for 33, 61 and 257 electrodes respectively. We report only the relative error on the source position e_{pos}. The first row of each figure (here and in the remaining of Section 5) corresponds to the

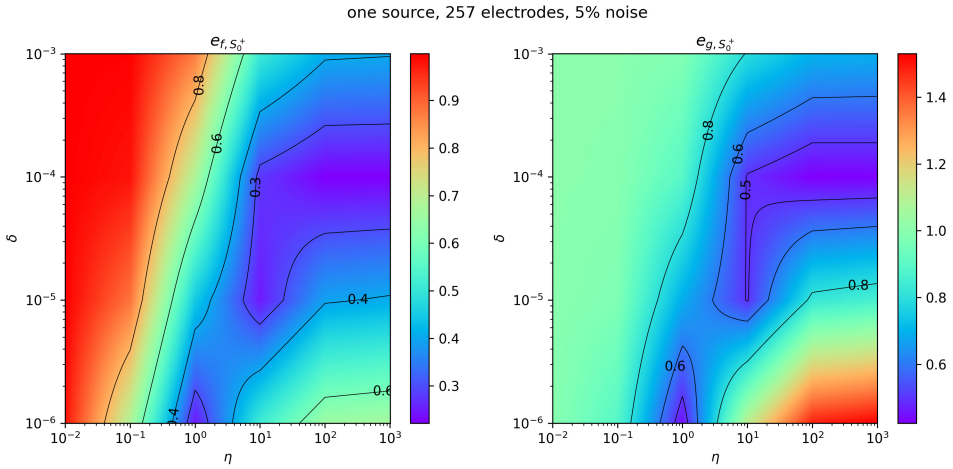

Figure 8. Relative L^2 error of the QR reconstruction in the Dirichlet (left) and Neumann (right) data at the cortex in the 257 electrodes case with 5% noise, for varying values of δ and η.

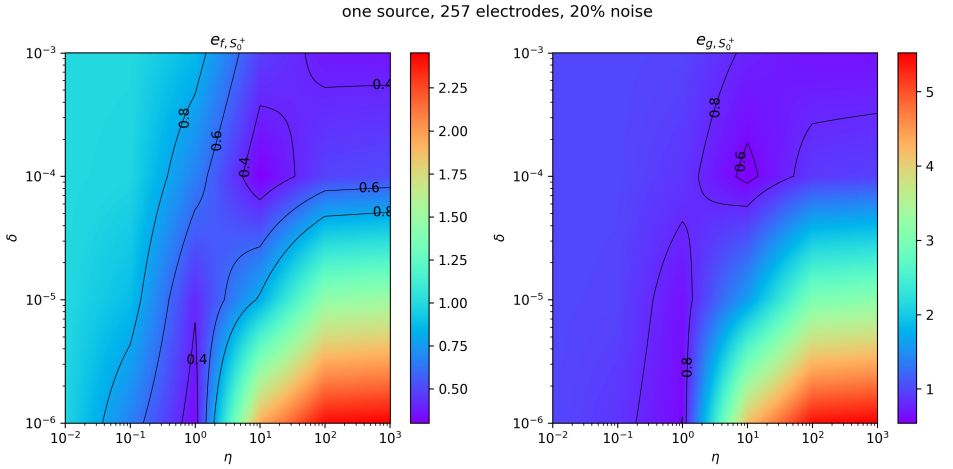

Figure 9. Relative L^2 error of the QR reconstruction in the Dirichlet (left) and Neumann (right) data at the cortex in the 257 electrodes case with 20% noise, for varying values of δ and η.

reference data simulated by solving the forward problem and the true source localisation. The characteristics of the source (location and orientation) are very accurately retrieved in each configuration. Best results are obtained for 257 electrodes. The impact of the electric brain source is visible on a specific area of the cortex (first row). Such a behaviour of the Cauchy data is still observed after the transmission process. Thus, knowing this information, the source reconstruction is efficient.

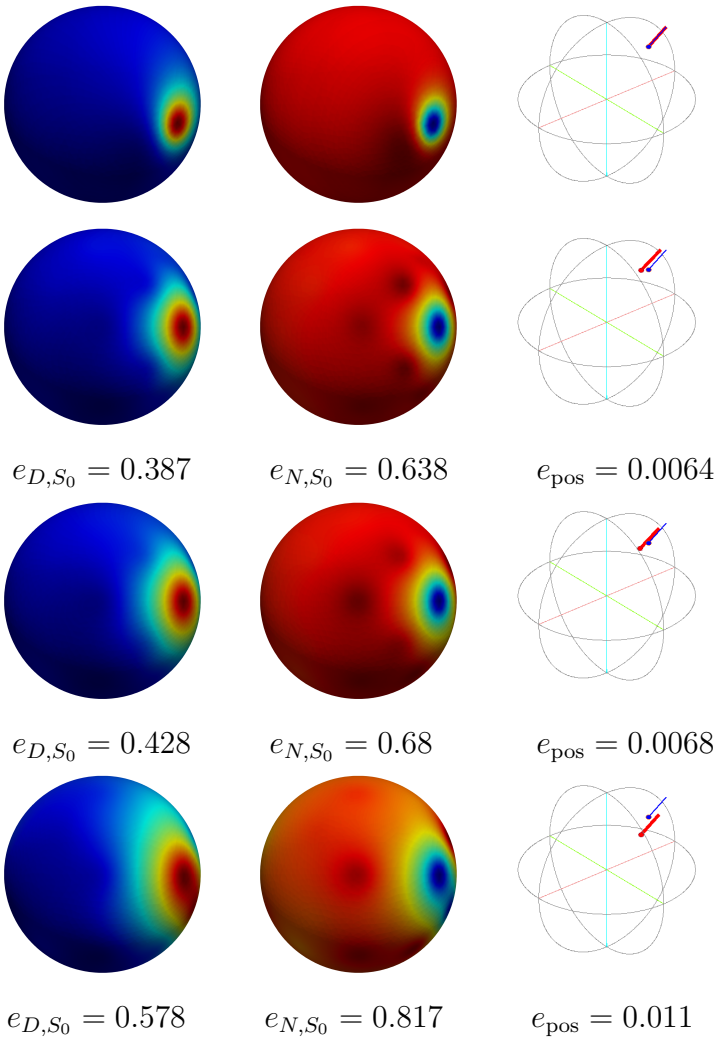

Figure 10. One distant source $(\boldsymbol{c}_{q_d}, \boldsymbol{p}_{q_d})$ and head model (a): QR reconstruction on the cortex with 33 electrodes and source reconstruction with FS3D. From top to bottom: exact solution, then reconstruction with 0%, 5% and 20% noise. From left to right: Dirichlet trace, Neumann trace, source reconstruction with FS3D.

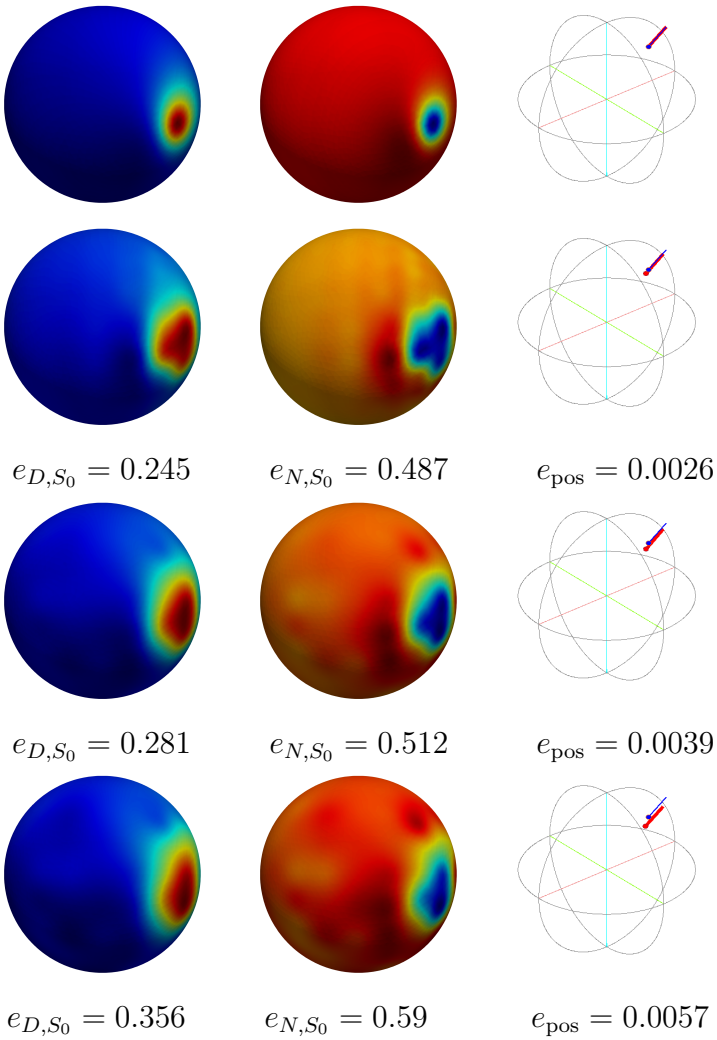

Figure 11. One distant source $(\boldsymbol{c}_{q_d}, \boldsymbol{p}_{q_d})$ and head model (a): QR reconstruction on the cortex with 61 electrodes and source reconstruction with FS3D. From top to bottom: exact solution, then reconstruction with 0%, 5% and 20% noise. From left to right: Dirichlet trace, Neumann trace, source reconstruction with FS3D.

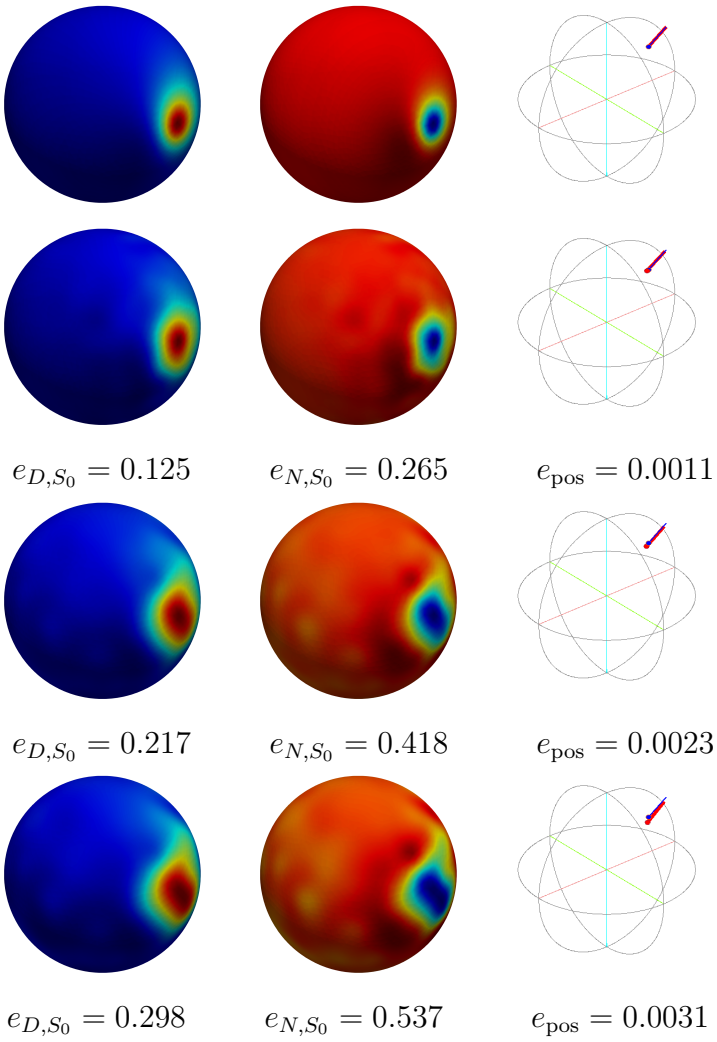

Figure 12. One distant source $(\boldsymbol{c}_{q_d}, \boldsymbol{p}_{q_d})$ and head model (a): QR reconstruction on the cortex with 257 electrodes and source reconstruction with FS3D. From top to bottom: exact solution, then reconstruction with 0%, 5% and 20% noise. From left to right: Dirichlet trace, Neumann trace, source reconstruction with FS3D.

5.4. Two distant sources, no fontanel

Here we consider the two symmetric distant sources $(\boldsymbol{c}_{q_d}, \boldsymbol{p}_{q_d})$ and $(\boldsymbol{c}_{q_{-d}}, \boldsymbol{p}_{q_{-d}})$. QR reconstructions on the cortex and source reconstruction with FS3D for noiseless data and noisy data with 5% and 20% white Gaussian noise on the value of the potential at each electrode are reported in Figure 13 for 257 electrodes. Here and throughout the rest of the paper, an asterisk (*) on the position error means that the position error corresponds to the best one-to-one pairings of true and reconstructed sources, even though the number of reconstructed sources is larger than the number of true sources. The QR method well captures qualitatively the two localized perturbations of the electric potential at the cortex corresponding to the two sources. Results are better for the Dirichlet trace of the reconstructed electric potential than for its Neumann trace. The coupling QR-FS3D provides very precise source localizations, even with noisy data.

5.5. Two close sources, no fontanel

We test now the challenging case of two symmetric close sources $(\boldsymbol{c}_{q_c}, \boldsymbol{p}_{q_c})$ and $(\boldsymbol{c}_{q_{-c}}, \boldsymbol{p}_{q_{-c}})$. The data are computed for the case of 257 electrodes. QR reconstructions on the cortex and source reconstruction with FS3D for noiseless data and noisy data are shown in Figure 14. Results are again concluding and the two sources are efficiently localized. Their orientations are also well retrieved. Even if the reconstruction errors after the data transmission are higher than for two distant sources, we can still distinguish the presence of two distinct electric activities at the cortex, which are associated with the two sources. The distinction is less easy for 20% noise.

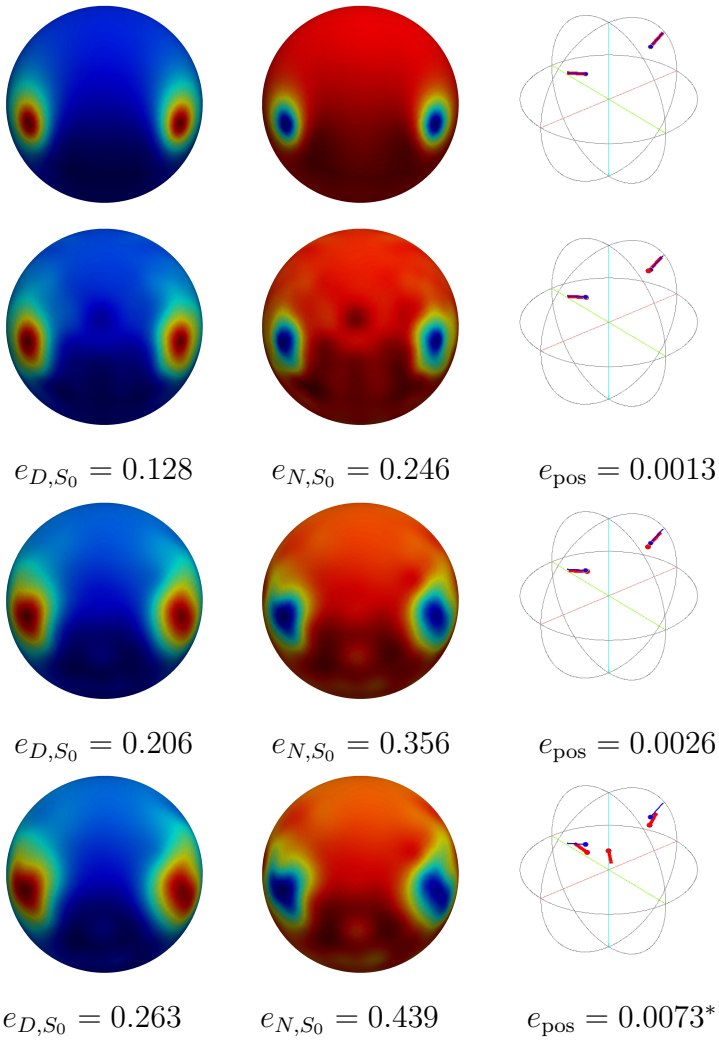

Figure 13. Two distant sources $(\boldsymbol{c}_{q_d}, \boldsymbol{p}_{q_d})$ and $(\boldsymbol{c}_{q_{-d}}, \boldsymbol{p}_{q_{-d}})$, head model (a): QR reconstruction on the cortex with 257 electrodes and source reconstruction with FS3D. From top to bottom: exact solution, then reconstruction with 0%, 5% and 20% noise. From left to right: Dirichlet trace, Neumann trace, source reconstruction with FS3D.

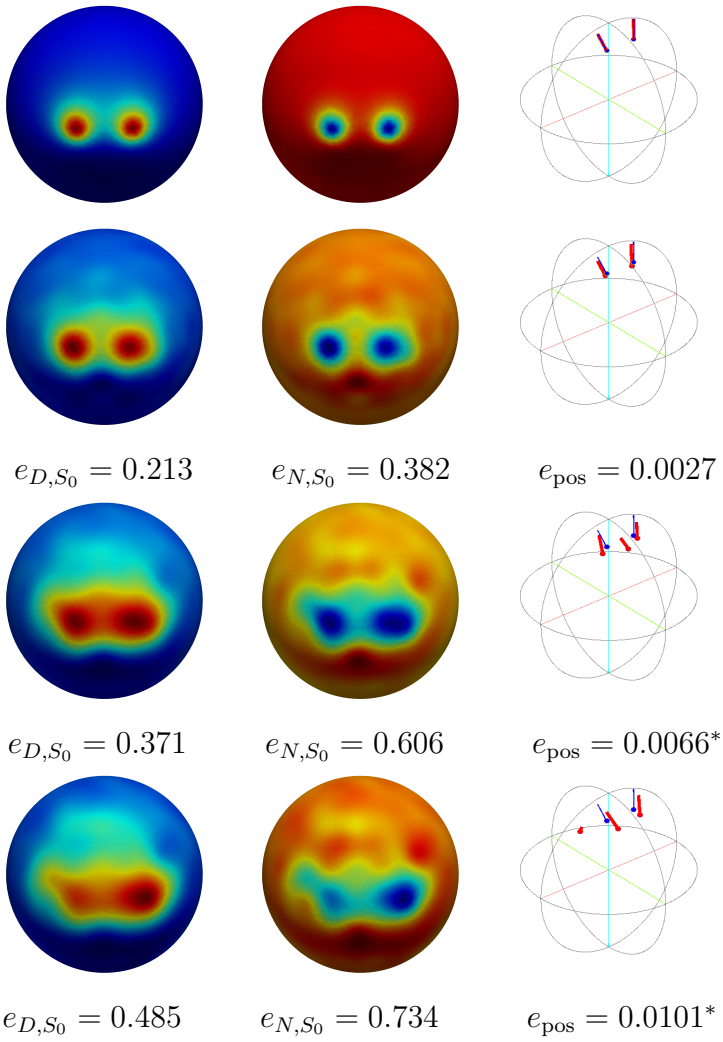

Figure 14. Two close sources $(\boldsymbol{c}_{q_c}, \boldsymbol{p}_{q_c})$ and $(\boldsymbol{c}_{q_{-c}}, \boldsymbol{p}_{q_{-c}})$ and head model (a): QR reconstruction on the cortex with 257 electrodes and source reconstruction with FS3D. From top to bottom: exact solution, then reconstruction with 0%, 5% and 20% noise. From left to right: Dirichlet trace, Neumann trace, source reconstruction with FS3D.

5.6. One source, CSF and fontanel

For these simulations, we consider the head model (b) including the main fontanel in the skull layer and a varying conductivity (29). We add also a 2mm cerebrospinal fluid (CSF) layer around the cortex. The CSF layer has high conductivity $\sigma_{\text{CSF}} = 1.8\text{S.m}^{-1}$. Figure 15 shows the mesh of such a domain. We perform the same previous tests with one close source $(\boldsymbol{c}_{q_c}, \boldsymbol{p}_{q_c})$ located close to the brain-CSF interface. The results are reported in Figure 16 and validate the approach in the case of a more realistic conductivity. The data transmission method is able to treat complex head models and is complementary with the reconstruction approach of FS3D. Here again, at the cortex surface, the QR method keeps the location of the support of the Dirichlet and Neumann traces which is useful for solving the inverse source problem.

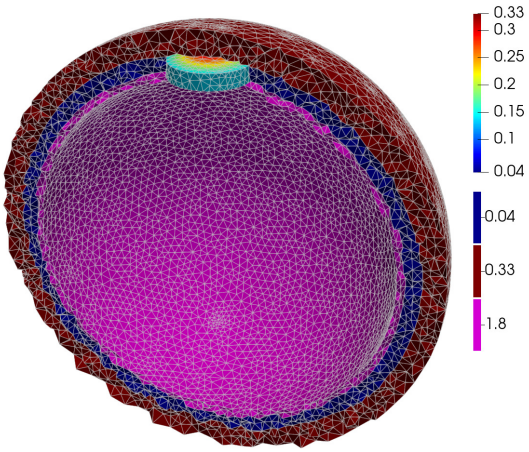

Figure 15. Mesh of the three conductivity regions around the cortex corresponding to CSF, skull and scalp, including the main fontanel region with varying conductivity.

5.7. Two close sources, CSF and fontanel

Finally, we test the reconstruction of the two symmetric close sources $(\boldsymbol{c}_{q_c}, \boldsymbol{p}_{q_c})$ and $(\boldsymbol{c}_{q_{-c}}, \boldsymbol{p}_{q_{-c}})$ using synthetic data generated with the head model (b) and CSF. Figure 17 compares what happens when not taking the fontanel into account in the QR reconstruction (columns 1-3), and when taking the fontanel into account (columns 4-6). For both cases, the sources are efficiently reconstructed. The method allows to treat a varying skull conductivity and is validated for such an heterogeneous medium. Results are quite similar with or without the anterior fontanel. Nevertheless, visually, it seems that the information associated with the two close sources is better reconstructed by the QR process with the presence of the fontanel, until 5% noise level. Fontanel would play a role in the localization of close sources for neonates from EEG measurements. We summarize all the results of the section in Table 1.

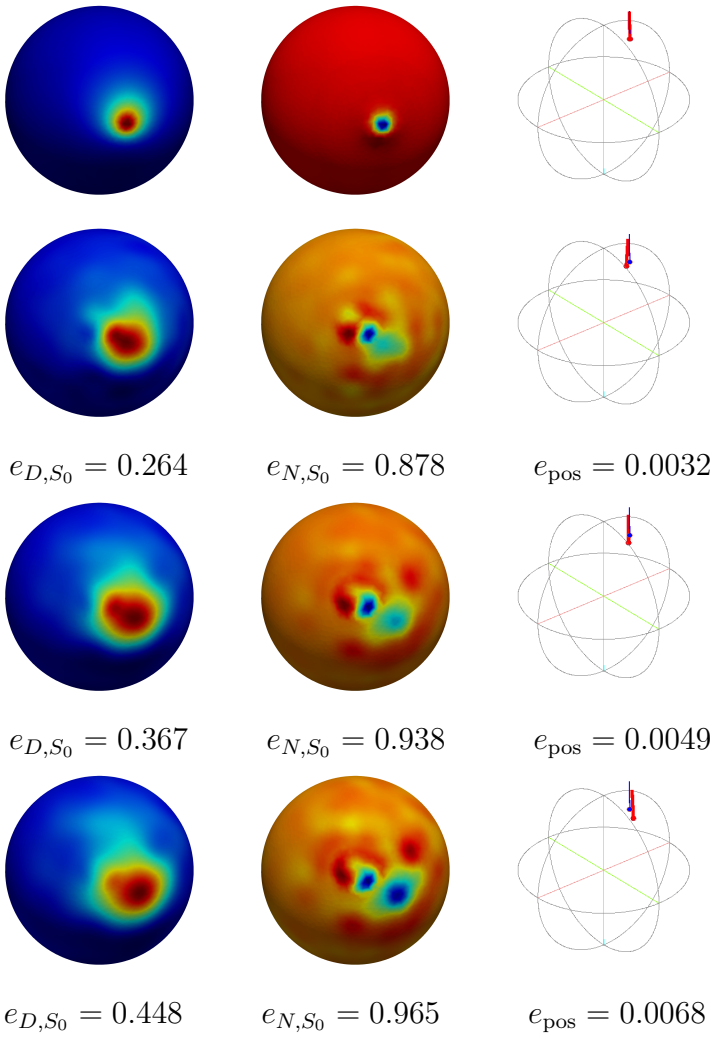

Figure 16. One close source $(\boldsymbol{c}_{q_c}, \boldsymbol{p}_{q_c})$, model (b) with CSF and fontanel: QR reconstruction on the cortex with 257 electrodes and source reconstruction with FS3D. From top to bottom: exact solution, then reconstruction with 0%, 5% and 20% noise. From left to right: Dirichlet trace, Neumann trace, source reconstruction with FS3D.

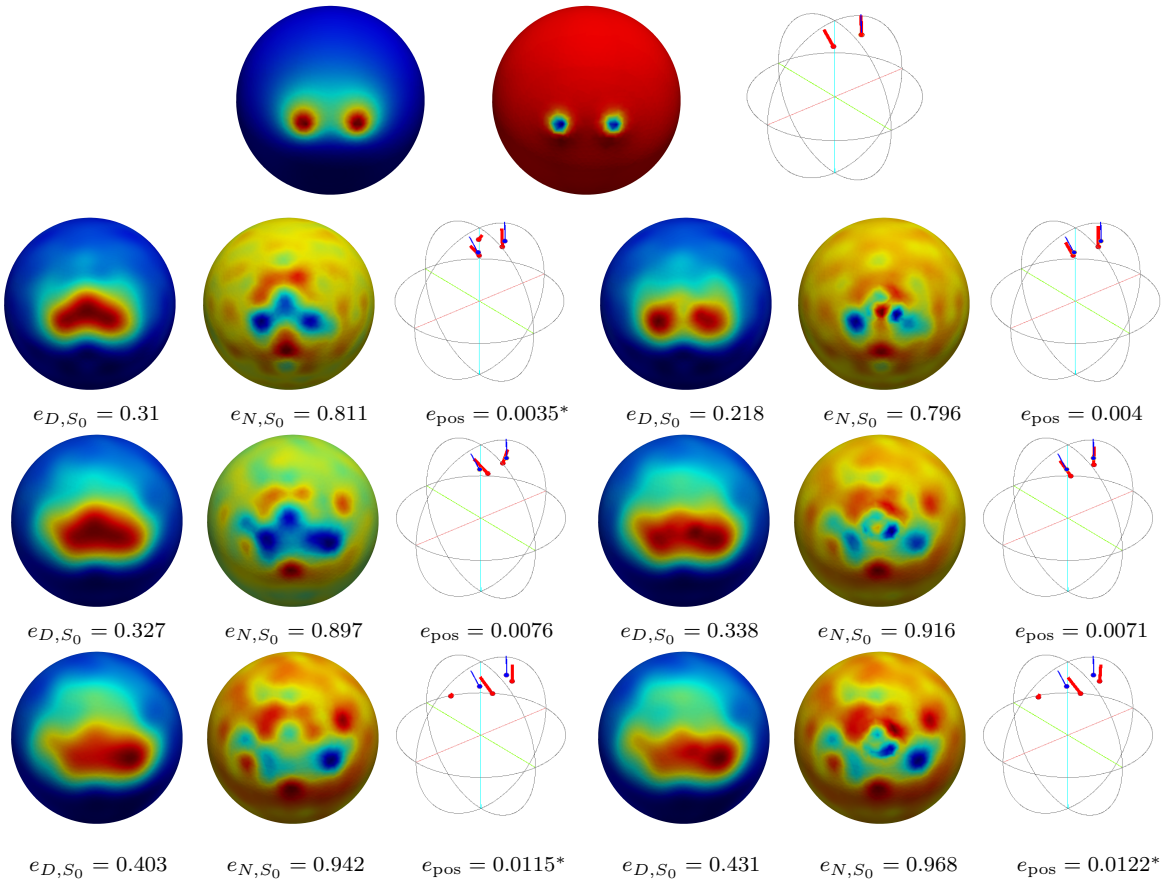

Figure 17. Two close sources $(\boldsymbol{c}_{q_c}, \boldsymbol{p}_{q_c})$ and $(\boldsymbol{c}_{q_{-c}}, \boldsymbol{p}_{q_{-c}})$, model (b) with CSF and fontanel: QR reconstruction on the cortex with 257 electrodes and source reconstruction with FS3D. Columns 1-3: without fontanel in the QR reconstruction; Columns 4-6: taking the fontanel into account. From top to bottom: exact solution, then reconstruction with 0%, 5% and 20% noise. From left to right: Dirichlet trace, Neumann trace, source reconstruction with FS3D.

			0% noise			5% noise			20% noise		
Sources	Head model	#E	e_{D,S_0}	e_{N,S_0}	e_{pos}	e_{D,S_0}	e_{N,S_0}	e_{pos}	e_{D,S_0}	e_{N,S_0}	e_{pos}
1 distant	(a)	33	0.387	0.638	0.0064	0.428	0.68	0.0068	0.578	0.817	0.011
1 distant	(a)	61	0.245	0.487	0.0026	0.281	0.512	0.0039	0.356	0.59	0.0057
1 distant	(a)	257	0.125	0.265	0.0011	0.217	0.418	0.0023	0.298	0.537	0.0031
2 distant	(a)	257	0.128	0.246	0.0013	0.206	0.356	0.0026	0.263	0.439	0.0073*
2 close	(a)	257	0.213	0.382	0.0027	0.371	0.606	0.0066*	0.485	0.734	0.0101*
1 close	(b) + CSF	257	0.264	0.878	0.0032	0.367	0.938	0.0049	0.448	0.965	0.0068
2 close	(b) + CSF	257	0.218	0.796	0.004	0.338	0.916	0.0071	0.431	0.968	0.0122*
2 close	same w/o font. in QR	257	0.31	0.811	0.0035*	0.327	0.897	0.0076	0.403	0.942	0.0115*

Table 1. Summary of reconstruction errors for each case. *Sources*: configuration of the sources (see Section 5.1). *Head model*: constant conductivity model (a) or presence of the anterior fontanel (b) and CSF. For the last row, data is generated with model (b) and CSF, but the anterior fontanel is not taken into account in the QR reconstruction model. $\#E$: number of electrodes. e_{D,S_0}, e_{N,S_0}: error in the reconstructed Dirichlet and Neumann data at the cortex S_0. e_{pos}: relative error on the source position.

6. Conclusion

This work presents results concerning EEG inverse source problems for spherical inhomogeneous head models, obtained from the joint use of two numerical methods, QR and FS3D. The QR method propagates external measures (taken at electrodes on the scalp) through inhomogeneous layers to an internal spherical surface, the boundary of a domain which contains unknown sources. The Cauchy data obtained on that surface are processed by FS3D to estimate dipolar sources. FS3D takes full advantage of the source locations being contained in a spherical domain.

Though it seems not to affect the source estimation, Neumann data on the cortex are not as accurately reconstructed as the Dirichlet trace in Section 5. This may be balanced by the transmission of Dirichlet data on another sphere within the brain, close to the cortex and containing the sources.

Such an additional transmission step will also be analysed in order to handle more realistic head geometries. Indeed, the QR method itself can provide data transmission in meshed complex geometries. Mixed geometries of the head, with general layers and an additional spherical domain included in the brain and enclosing unknown sources could be considered.

Another development will be the processing of time varying records of EEG/MEG signal. FS3D is yet equiped for time/space separation of asynchronous sources.

A further interesting perspective would be to propose numerical (iterative) methods for

a simultaneous reconstruction of tissue conductivities and electric brain sources. It would allow for patient-specific EEG [39].

7. Appendix

Related to Section 4 and to the Step 2 of the source estimation process, for a fixed circle $T_{d,p}$, back to (26), we put

$$\tilde{u}^2(\boldsymbol{x}_{d,p}) = f_{d,p}(z) \text{ for } \boldsymbol{x}_{d,p} \simeq z \in T_{d,p} \subset \mathbb{R}^2 \simeq \mathbb{C}\,,$$

as we now precise. To illustrate, take for $d = 1$ the direction corresponding to circles $T_{1,p} = T_p$ orthogonal to the vertical axis $(0\,x_3)$, in the horizontal planes $\Pi_{1,p} = \Pi_p = \{x_3 = x_{3,p}\}$, of radius $r_p = \sqrt{r_0^2 - x_{3,p}^2}$.

3D-2D mapping of the 3D data On such a circle T_p, we identify the first two coordinates with their associate complex affix $z \in \mathbb{T}$:

$$\boldsymbol{x}_{1,p} = \boldsymbol{x}_p = (x_1, x_2, x_{3,p}) \;\leftrightarrow\; z = \frac{x_1 + i\,x_2}{r_p}\,,\; |z| = 1\,. \tag{30}$$

In fact, these formula identify the whole plane Π_p with the complex plane $\mathbb{C}$, and maps back any point inside the unit disk $\mathbb{D}$ onto a point in the interior of the disk D_p with boundary T_p in Π_p .

Let us explicit this inverse mapping for the singularities of $f_{d,p}$. With $\boldsymbol{c}_q = (x_{1,q}, x_{2,q}, x_{3,q})$, $z_q = x_{1,q} + i\,x_{2,q}$ (in D_p), $h_{p,q} = x_{3,p} - x_{3,q}$, we have

$$|\boldsymbol{x}_p - \boldsymbol{c}_q|^2 = (x_1 - x_{1,q})^2 + (x_2 - x_{2,q})^2 + h_{p,q}^2 = |r_p\,z - z_q|^2 + h_{p,q}^2$$

$$= (r_p\,z - z_q)\,(r_p\,\bar{z} - \bar{z}_q) + h_{p,q}^2 = (r_p\,z - z_q)\,(\frac{r_p}{z} - \bar{z}_q) + h_{p,q}^2\,,$$

on T_p, since $1 = |z|^2 = z\,\bar{z}$, whence $\bar{z} = 1/z$. Hence, assuming $z_q \neq 0$, we get on T_p,

$$|\boldsymbol{x}_p - \boldsymbol{c}_q|^2 = -\frac{r_p\,\bar{z}_q}{z}\,\left(z^2 - \frac{h_{p,q}^2 + |z_q|^2 + r_p^2}{r_p\,\bar{z}_q}\,z + \frac{z_q}{\bar{z}_q}\right)\,.$$

Next, we have

$$z^2 - \frac{h_{p,q}^2 + |z_q|^2 + r_p^2}{r_p\,\bar{z}_q}\,z + \frac{z_q}{\bar{z}_q} = (z - s_{p,q})\;(z - t_{p,q})$$

with

$$s_{p,q} \in \mathbb{D}\,,\; t_{p,q} \in \mathbb{C} \setminus \overline{\mathbb{D}}\,,\; |s_{p,q}|\;|t_{p,q}| = 1\,,\; \arg s_{p,q} = \arg t_{p,q} = \arg z_q\,.$$

The argument $\arg s_{p,q}$ of the root $s_{p,q} \in \mathbb{D}$ is thus independent of p, and equal to the argument of z_q (allows to estimate Q and to discriminate between different z_q). Actually,

$$s_{p,q} = \frac{z_q}{2\,|z_q|^2\,r_p}\,\left(h_{p,q}^2 + |z_q|^2 + r_p^2 - \sqrt{\left(h_{p,q}^2 + (r_p - |z_q|)^2\right)\,\left(h_{p,q}^2 + (r_p + |z_q|)^2\right)}\right)\,. \tag{31}$$

2D-3D mapping of the 2D singularities We have $s_{p,q} = \rho_p\, z_q/r_p$ with ρ_p a real positive function of $x_{3,p} \in (-r_0, r_0)$. The function ρ_p increases monotonically for $-r_0 < x_{3,p} < x_{3,q}$ ($h_{p,q} < 0$), decreases monotonically for $x_{3,q} < x_{3,p} < r_0$ ($h_{p,q} > 0$), and attains a maximum when $x_{3,p} = x_{3,q}$ ($h_{p,q} = 0$), in which case one has $\rho_p(x_{3,p}) = 1$ and $r_p\, s_{p,q} = z_q$ which, back to Ω_0, coincides with the source location $\boldsymbol{c}_q$.
Due to this behavior of the roots $s_{p,q} \in \mathbb{D}$, specifically of their argument $\arg s_{p,q} = \arg z_q$, $\forall p = 1, \cdots, P$, and of the modulus $|r_p\, s_{p,q}|$ which reaches its maximal value at $x_{3,p} = x_{3,q}$, we see that recovering the $s_{p,q}$, $\forall p = 1, \cdots, P$, allows one to estimate both z_q and $x_{3,q}$, whence $\boldsymbol{c}_q$.
For fixed d, p, $s_{d,p,q}$ correspond to the Q singularities in $\mathbb{D}$ of the function f_p defined by (see (27)):

$$f_p(z) = f_{d,p}(z) = \sum_{q,k=1}^{Q} \frac{\varphi_{p,q}(z)\, \varphi_{p,k}(z)}{(z - s_{p,q})^{3/2}\, (z - s_{p,k})^{3/2}}\,.$$

The functions $\varphi_{p,q}$ in $\mathbb{D}$ above and at the numerators in (27), (28) are as follows. If $\boldsymbol{p}_q = (p_{1,q}, p_{2,q}, p_{3,q})$, set $p_q = p_{1,q} + i\, p_{2,q}$, then

$$\varphi_{p,q}(z) = \frac{1}{8\,\pi}\, \frac{\bar{p}_q}{(r_p\, \bar{z}_q)^{3/2}}\, \frac{\sqrt{z}}{(z - t_{p,q})^{3/2}}\, \pi_{p,q}(z)\,,$$

for polynomials $\pi_{p,q}$ of degree 2:

$$\pi_{p,q}(z) = r_p\, z^2 + 2\frac{p_{3,q}\, h_{p,q} - \mathrm{Re}\,(z_q\, \bar{p}_q)}{\bar{p}_q}\, z + \frac{p_q}{\bar{p}_q}\, r_p\,.$$

Finally, observe that situations where $z_q = 0$ are degenerate. Except if $\boldsymbol{c}_q = 0$, they may only occur in some directions d. Whenever $z_q = 0$, the corresponding term in (27) is polynomial and does not admit singularities. This could be detected by the rational approximation step of the algorithm.

[1] M. Antonakakis, S. Schrader, U. Aydin, A. Khan, J. Gross, M. Zervakis, S. Rampp, C.H. Wolters, *Inter-Subject Variability of Skull Conductivity and Thickness in Calibrated Realistic Head Models*, Neuroimage, **223** (2020), 117353.

[2] B. Atfeh, L. Baratchart, J. Leblond, J.R. Partington *Bounded extremal and Cauchy-Laplace problems on the sphere and shell*, J. Fourier Analysis and Applications, **16**(2) (2010), 177–203.

[3] H. Azizollahi, M. Darbas, M. Diallo, A. El Badia, S. Lohrengel, *EEG in neonates: forward modeling and sensitivity analysis with respect to variations of the conductivity*, Mathematical Biosciences and Engineering, **15**(4) (2018), 905–932.

[4] L. Baratchart, A. Ben Abda, F. Ben Hassen, J. Leblond, *Recovery of pointwise sources or small inclusions in 2D domains and rational approximation*, Inverse Problems, **21** (2005), 51–74.

[5] L. Baratchart, L. Bourgeois, J. Leblond, *Uniqueness results for inverse Robin problems with bounded coefficients*, J. Functional Analysis, **270**(1) (2016), 2508–2542.

[6] S.R. Benbadis, S. Beniczky, E. Bertram, S. MacIver, S. L. Moshé, *The role of EEG in patients with suspected epilepsy*, Epileptic Disord **22**(2) (2020), 143–155.

[7] L. Bourgeois, *A mixed formulation of quasi-reversibility to solve the Cauchy problem for Laplace's equation*, Inverse Problems, **21** (2005), 1087–1104.

[8] L. Bourgeois, L. Chesnel, *On quasi-reversibility solutions to the Cauchy problem for the Laplace equation: regularity and error estimates*, Math. Mod. Num. Anal., **54** (2020), 493–529.

[9] L. Bourgeois, J. Dardé, *A duality-based method of quasi-reversibility to solve the Cauchy problem in the presence of noisy data*, Inverse Problems, **26**(9) (2010), 095016.

[10] L. Bourgeois, A. Recoquillay, *A mixed formulation of the Tikhonov regularization and its application to inverse PDE problems*, Mathematical Modelling and Numerical Analysis, **52**(1) (2018), 123–145.

[11] M. Clerc, J. Leblond, J.-P. Marmorat, T. Papadopoulo, *Source localization in EEG using rational approximation on plane sections*, Inverse Problems **28** (2012), 055018.

[12] M. Clerc, J. Leblond, J.-P. Marmorat, C. Papageorgakis, *Uniqueness result for an inverse conductivity recovery problem with application to EEG*, Rendiconti dell'Istituto di Matematica dell'Università di Trieste. An International Journal of Mathematics (2016), 48.

[13] C. Dapogny, C. Dobrzynski, P. Frey, *Three-dimensional adaptive domain remeshing, implicit domain meshing, and applications to free and moving boundary problems*, Journal of Computational Physics **262** (2014), 358–378.

[14] M. Darbas, M. Diallo, A. El Badia, S. Lohrengel, *An inverse dipole source problem in inhomogeneous media: application to the EEG source localization in neonates*, Journal of Inverse and Ill-Posed Problems, **27**(2) (2019), 255–282.

[15] M. Darbas, S. Lohrengel, *Review of mathematical modeling of electroencephalography (EEG)*, Jahresbericht der Deutschen Mathematiker-Vereinigung, **121**(1) (2019), 3–39.

[16] J. Dardé, *Méthodes de quasi-réversibilité et de lignes de niveau appliquées aux problèmes inverses elliptiques*, Thèse de doctorat, Université Paris-Diderot, 2010.

[17] J. Dardé, *Iterated quasi-reversibility method applied to elliptic and parabolic data completion problems*, Inverse Problems and Imaging, **10**(2), (2016), 379–407.

[18] R. Dautray, J.-L. Lions, *Mathematical Analysis and Numerical Methods for Science and Technology*, Vol. 1, Springer, 2000.

[19] A. Delorme, S. Makeig, *EEGLAB: an open source toolbox for analysis of single-trial EEG dynamics including independent component analysis*, J. Neuroscience Methods, **134**(1), (2004).

[20] M. M. Diallo, *Problème inverse de sources en Electro-Encéphalo-Graphie chez le nouveau-né*, Thèse de doctorat, Université de Picardie Jules Verne, France, 2017.

[21] A. El Badia, T. Ha Duong, *An inverse source problem in potential analysis*, Inverse Problems, **16** (2000), 651–663.

[22] I. Gaudet, A. Hüsser, P. Vannasing, A. Gallagher, *Functional Brain Connectivity of Language Functions in Children Revealed by EEG and MEG: A Systematic Review*, Front. Hum. Neurosci **14**:62 (2020).

[23] A. Gramfort, T. Papadopoulo, E. Olivi, M. Clerc, *OpenMEEG: opensource software for quasistatic bioelectromagnetics*, BioMedical Engineering OnLine, **45** (2010).

[24] R. Grech, T. Cassar, J. Muscat, K.P. Camilleri, S.G.Fabri, M. Zervakis, P. Xanthopoulos, V. Sakkalis, B. Vanrumste, *Review on solving the inverse problem in EEG source analysis*, J. Neuro. Rehabil. **5**(25) (2008), 1–33.

[25] J. Hadamard, *Sur les probèmes aux dérivées partielles et leur signification physique*, Princeton University Bulletin, **13**(4), (1902), 49-52.

[26] M. Hämäläinen, R. Hari, J. Ilmoniemi, J. Knuutila, O.V. Lounasmaa, *Magnetoencephalography-theory, instrumentation, and applications to noninvasive studies of the working human brain*, Rev. Mod. Phys., **65** (1993), 413–497.

[27] F. Hecht, *New Development in FreeFem++*, *Journal of Numerical Mathematics* **20**(3-4) (2012), 251–

265.

[28] J. D. Jackson, *Classical Electrodynamics*, Third edition, John Wiley & Sons, 1998.

[29] M. V. Klibanov, F. Santosa, *A computational quasi-reversibility method for cauchy problems for Laplace's equation*, SIAM J. Appl. Math., **51** (1991), 1653–1675.

[30] V.A. Kozlov, V.G. Mazya, A.V. Fomin, *An iterative method for solving the Cauchy problem for elliptic equation*, Comput. Math. Phys., **31** (1991), 45–52.

[31] R. Kress, *Linear Integral Equations*, Second edition, Applied Mathematical Sciences 82, Spinger-Verlag, 1999.

[32] R. Lattès, J.-L. Lions, *Méthode de Quasi-réversibilité et Applications*, Dunod, Paris, 1967.

[33] J. Leblond, C. Paduret, S. Rigat, M. Zghal, *Source localization in ellipsoids by best meromorphic approximation in planar sections*, Inverse Problems, **24**(3) (2008), 035017.

[34] F.-H. Lin, J.W. Belliveau, A.M. Dale, M. Hämäläinen, *Distributed current estimates using cortical orientation constraints*, Human Brain Mapp., **27**(1) (2006).

[35] J.C. Mosher, R.M. Leahy, *Recursive MUSIC: a framework for EEG and MEG source localization*, IEEE Trans IEEE Trans. on Biomed. Eng., **45**(11) (1998).

[36] J.C. Mosher, R.M. Leahy, P.S. Lewis, *EEG and MEG: forward solutions for inverse methods*, IEEE Trans. on Biomed. Eng., **46** (1999), 245–259

[37] J. C. de Munck, M. J. Peters, *A fast method to compute the potential in the multisphere model*, IEEE Trans. Biomed. Eng. **40** (1993), 1166–1174.

[38] D. Nikodijevic, N. Baneva-Dolnenec, D. Petrovska-Cvetkovska, D. Caparoska, *Refractory Epilepsy-MRI, EEG and CT scan, a Correlative Clinical Study*, Open Access Maced J Med Sci. **4**(1) (2016), 98–101.

[39] C. Papageorgakis, *Patient specific conductivity models: characterization of the skull bones*, PhD Thesis, Université Côte d'Azur, France, 2017.

[40] J. Pescatore, I. Bloch, S. Baillet, L. Garnero, *F.E.M. tetrahedral mesh of head tissues from M.R.I. under geometrical and topological constraints for applications in E.E.G. and M.E.G.*, NeuroImage **13**(6) (2001), 218.

[41] N. Roche-Labarbe, A. Aarabi, G. Kongolo, C. Gondry-Jouet, M. Dümpelmann, R. Grebe, F. Wallois, *High-resolution electroencephalography and source localization in neonates*, Human Brain Mapping, **29** (2008), 167–176.

[42] J. Le Rousseau, G. Lebeau, *On Carleman estimates for elliptic and parabolic operators. Applications to unique continuation and control of parabolic equations*, ESAIM: Control, Optimisation and Calculus of Variations, **18**(3) (2012), 712–747.

[43] M. Salo, *Unique continuation for elliptic equations*, Notes, Fall, University of Jyväskylä (2014).

[44] M. Schneider, *A multistage process for computing virtual dipole sources of EEG discharges from surface information*, IEEE Trans. on Biomed. Eng., **19** (1972), 1–12.

[45] F. Wallois, L. Routier, C. Heberlé, M. Mahmoudzadeh, E. Bourel-Ponchel, S. Moghimi, *Back to basics: the neuronal substrates and mechanisms that underlie the electroencephalogram in premature neonates*, Neurophysiol Clin. **51**(1)(2021), 5–33.

[46] C.H. Wolters, H. Köstler, C. Möller, J. Härdtlein, L. Grasedyck, W. Hackbusch, *Numerical mathematics of the subtraction approach for the modeling of a current dipole in EEG source reconstruction using finite element head models*, SIAM J. Sci. Comput., **30**(1) (2007), 24–45.